



1 **The role of pre-existing jointing on damage zone evolution and faulting style of thin**
2 **competent layers in mechanically stratified sequences: a case study from the Limestone Coal**
3 **Formation at Spireslack Surface Coal Mine.**

4 Billy J. Andrews*, Zoe K. Shipton, Richard Lord, Lucy McKay
5

6 Department of Civil and Environmental Engineering, University of Strathclyde, Glasgow, G11XJ,
7 Scotland

8 *Correspondence to:* Billy J. Andrews (billy.andrews@strath.ac.uk)

9 **Abstract.** Fault and fracture networks play an important role in sub-surface fluid flow and can act to
10 enhance, retard or compartmentalise groundwater flow. In multi-layered sequences, the internal structure
11 and growth of faults is not only controlled by fault throw, but also the mechanical properties of lithologies
12 cut by the fault. This paper uses geological fieldwork, combined with fault and fracture mapping, to
13 investigate the internal structure and fault development of the mechanically stratified Limestone Coal
14 Formation and surrounding lithologies exposed at Spireslack Surface Coal Mine. We find that the
15 development of fault rock, and complexity of a fault zone is dependent on: a) whether a fault is self-
16 juxtaposed or cuts multiple lithologies; b) the presence and behaviour of shale, which can lead to
17 significant bed-rotation and the formation of fault-core lenses; and c) whether pre-existing weakness (e.g.
18 joints) are present at the time of faulting. Pre-existing joint networks in the McDonald Limestone, and
19 cleats in the McDonald Coal, influenced both fault growth and fluid flow within these lithologies.

20 **1 Introduction**

21 The mechanical properties, thickness, and interface properties of lithologies in a stratigraphic succession,
22 referred to as mechanical stratigraphy, combine to influence the deformation style of a rock mass (e.g.
23 Ferrill *et al.* (2017)). The effect of mechanical stratigraphy on faulting, in particular normal faulting, has
24 been studied for sand-shale sequences (e.g. van der Zee & Urai (2005); Schmatz *et al.* (2010)),
25 interbedded limestones and marls (e.g. Ferrill & Morris (2003), (2008); Long & Imber (2011); Ferrill *et*
26 *al.* (2012)), and ignimbrites (Soden and Shipton, 2013). The lithology being cut by the fault influences
27 fault dip: strands in competent layers have steeper dips than those in incompetent layers (Ferrill and
28 Morris, 2008). The ratio of competent to incompetent lithologies thus affects fault style and displacement
29 profiles (Ferrill *et al.*, 2017; Ferrill and Morris, 2008). When incompetent layers dominate the sequence,
30 folding is commonly observed with thin competent beds displaying fault-related folding (Ferrill and
31 Morris, 2008; Lăpădat *et al.*, 2017). The presence of incompetent lithologies also restricts fault growth
32 with strands terminating at incompetent beds. This leads to faults with high aspect ratios orientated



33 parallel to the strike of bedding (e.g. Nicol *et al.* (1996); Soliva & Benedicto (2005); Roche *et al.* (2013)).
34 In addition to mechanical stratigraphy, pre-existing weaknesses play an important role in the nucleation
35 and development of faulting (Crider and Peacock, 2004). The impact pre-existing weaknesses have on
36 fault growth depends on the orientation of a weakness relative to the growing fault and the stress ratio
37 (Lunn *et al.*, 2008; Peacock, 2001). The presence of pre-existing weaknesses can also influence the
38 development of fault rock. For example, Soden & Shipton (2013) demonstrated that layer and joint
39 spacing in ignimbrites affected the aspect ratio of clasts found within the fault core. Of course, mechanical
40 stratigraphy itself influences the orientation of pre-existing weaknesses (Wilkins and Gross, 2002).

41 Fluvial-deltaic sequences are characterised by cyclical sequences of limestone, sandstone, siltstone, seat-
42 earth, shale, and coal (Thomas, 2013). The competent lithologies in the sequence (limestone and
43 sandstone) commonly contain joints. Coal has a unique, distinctive blocky texture due to the presence of
44 two roughly perpendicular fracture sets called cleats (Laubach *et al.*, 1998). Cleats are ubiquitous in coals
45 as diagenesis takes place, and thus represent pre-existing weaknesses which may affect the location,
46 orientation and length of faults (e.g. Peacock (2001); Walsh *et al.* (2002)).

47 This study utilises exceptional exposures of the Limestone Coal Formation (LCF) exposed at Spireslack
48 Surface Coal Mine (SCM), Scotland, to investigate the effect of lithology and pre-existing structures on
49 the growth of strike-slip faults. Field photographs were used to map the key structures and kinematics at
50 a 1:1,000 scale. High resolution photomontages were then used to map faults and fractures and investigate
51 the interaction of faults and fractures with lithology and jointing. We find that faults cutting multiple
52 lithologies are thin (<0.3 m), display a complex deformation pattern, and locally branch entraining lenses
53 of sandstone. We also find that pre-existing joints and lithology strongly affect the growth and fluid flow
54 history of small offset, self-juxtaposed, faults.

55 **2. Geological setting**

56 The Midland Valley of Scotland (MVS) is a 90 km wide, 150 km long, ENE-trending basin that opened
57 during the late Devonian to Early Carboniferous in response to back-arc extension within the Laurussian
58 Plate (Leeder, 1982, 1988). This was followed by a period of thermal subsidence which continued
59 throughout Namurian and Westphalian times leading to the deposition and preservation of thick coal
60 measures across much of the UK (Leeder, 1982; Figure 1a).

61 The MVS is bound by two major tectonic lineaments - the Southern Upland Fault (SUF) to the south and
62 Highland Boundary Fault (HBF) to the north (Figure 1a) (Bluck, 1984). Carboniferous basins that have
63 axes oblique to the main trend of the MVS (e.g. Central Scottish Coalfield; Francis (1991)). These basins
64 can reach over 6 km in thickness (Dean *et al.*, 2011) and are often obscured by Quaternary deposits. Faults

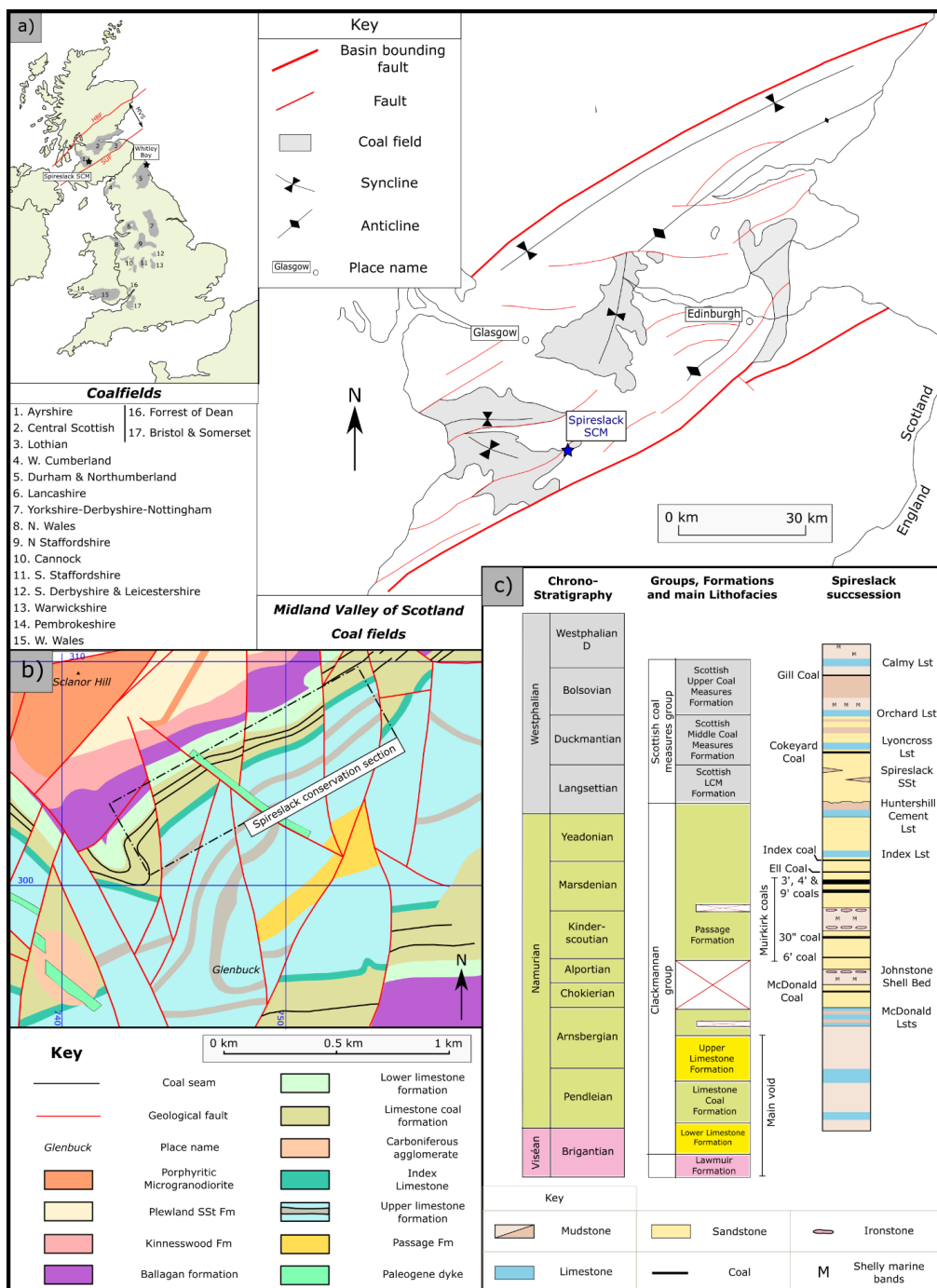


65 with associated, localised folding within the MVS have a complex history of reactivation caused by
66 sinistral strike-/oblique-slip during the Tournaisian and dextral strike-/oblique-slip during Viséan to
67 Westphalian times (Browne and Monro, 1987; Rippon et al., 1996; Ritchie et al., 2003; Underhill et al.,
68 2008).

69 **2.1 Spireslack SCM**

70 Spireslack SCM, next to the now abandoned coal mining village of Glenbuck, South Ayrshire, Scotland
71 (Figure 1a) provides an exceptional exposure of Carboniferous rocks in a 1 km long void (Figure 1b). A
72 20°- 40° southerly dipping slope along bedding planes ends in a <130 m high working face. The
73 stratigraphy, comprises a continuous succession of Viséan to Namurian strata including a complete
74 section through the Limestone Coal Formation (LCF) (Figure 1c) (Ellen et al., 2016, 2019). Bituminous
75 coal is found in cyclical fluvio-deltaic sequences that outcrop across much of the dip-slope and high wall,
76 bounded by the Upper and Lower Limestone Formations. The Lower Limestone Formation represents
77 more marine-influenced facies including extensive, fossil-rich limestone units (e.g. The McDonald
78 Limestone) (Davis, 1972). Above the LCF the Spireslack Sandstone comprises of one channelised, and
79 two tabular, sandstone beds (Ellen et al., 2019).

80 Offsetting this stratigraphy are several fault zones with shallow slip vectors and variably complex internal
81 structures. In addition to the faults, at least five Paleogene basaltic dykes are observed, which Leslie *et*
82 *al.* (2016) suggest intrude along pre-existing faults. The rocks exposed at Spireslack SCM are part of the
83 Southern Limb of the upright, WSW-ENE trending Muirkirk syncline that formed in response to mid- to
84 late- Carboniferous sinistral transpression (Davis, 1972; Leslie et al., 2016). Leslie *et al.* (2016) attribute
85 the faulting and folding observed at Spireslack SCM to this deformation, and have observed no evidence
86 of the later widespread dextral deformation (e.g. Underhill *et al.* (2008)).



87

88 **Figure 1: Location map: a) Map of UK coalfields (adapted from Donnelly (2006)) showing the**
 89 **location of Spireslack SCM and Structural features of the Midland Valley of Scotland; b) Regional**
 90 **geology of Spireslack open cast coal mine (after Ellen et al. (2019)); c) Regional stratigraphy of**
 91 **Spireslack SCM (after Ellen et al. (2019)).**



92 **3. Methods**

93 **3.1. Field mapping**

94 Geological mapping of the dip-slopes captured all units between the sandstones and shales below the
95 McDonald Limestones and the sandstone bed above the Muirkirk 6' Coal. Mapping was undertaken at a
96 1:1,000 scale onto printed aerial photography from Bing (2017). All faults with greater than 0.2 m offset
97 were recorded. Printed field photographs were used to collect more detailed observations at several key
98 sites.

99 **3.2 Analysis of fault and fracture networks**

100 **3.2.1 Mapping procedure**

101 Fault and fracture mapping was undertaken using two datasets: (i) a UAV derived photomontage of the
102 McDonald Limestone bedding plane collected by Dave Healy of Aberdeen University; and (ii) an auto
103 rectified photomontage of the high wall collected by the British Geological Survey. Interpretation areas
104 were selected from the dip-slope and high wall for analysis to understand the geometrical and topological
105 properties, and cross cutting relationships of fault strands and joint sets. Due to the instability of the
106 highwall, there was very little access to the foot of the highwall and the interpretations are made
107 principally on the photomontage. The interpretation areas were scaled in ArcGIS with mapping being
108 undertaken by the lead author at a scale of 1:30 for the dip-slope and 1:50 for the high wall. Lineament
109 mapping was undertaken by the same operator, at the same scale, to limit the effect of subjective bias on
110 the data collected (Andrews et al., 2019; Scheiber et al., 2015).

111 **3.2.2 Network analysis**

112 Fracture topology describes a fault or fracture network as a series of branches and nodes (e.g. Manzocchi
113 (2002); Sanderson & Nixon (2015),(2018)). A branch is a fracture trace with a node at each end. Nodes
114 can occur where a fracture terminates into rock (i-node), abuts against another fracture (y-node) or crosses
115 another fracture (x-node). The proportion of different node types (i, y, and x) can then be plotted on a
116 triangular diagram for the purposes of characterising and quantifying the connectivity of the network
117 (Manzocchi, 2002; Sanderson and Nixon, 2015). In this work we interpret fault and fractures as
118 orientation sets and report fracture/branch trace length (tl), 2D fracture intensity (I), and the percentage
119 of connected branches (Pc).

120 Once the faults and fractures were interpreted (digitised as separate datasets), a visual assessment of the
121 network was undertaken followed by network analysis using the open source ArcGIS toolbox NetworkGT
122 (Nyberg et al., 2018) and the following workflow:



- 123 1. *Define sets*: Six ‘Interpretation boxes’ were added as shape files to the ArcGIS (three along the
124 dip-slope and three along the high wall) and the orientation of faults and the fractures within
125 them analysed. Length-weighted rose diagrams with 5° bin widths were used to interpret the
126 ‘orientation sets’ in the network using NetworkGT (Nyberg et al., 2018). The digitised fault and
127 fracture data sets were then combined using the merge function in ArcGIS, and all three
128 investigated separately.
- 129 2. *Branch & Nodes*: The topology of the network was extracted using the ‘Branch and Node’ tool,
130 which splits the fracture trace poly-line file into individual branches, and assigns nodes as a
131 separate point-files (Nyberg et al., 2018). The resulting network was visually checked for errors
132 (e.g. incorrectly assigned nodes) and manually adjusted in ArcGIS to remove spurious nodes and
133 branches. Data were then exported to excel for further analysis.
- 134 3. *Network analysis*: For each network, the following data was extracted;
- 135 a. *Network connectivity*: For each dataset with the data not split into sets, the node and
136 branch proportions were assessed using a triangular diagram (c.f. Sanderson & Nixon
137 (2015)). The percentage of connected branches was then calculated using Equation 1.

138
$$P_c = \frac{(3N_y + 4N_x)}{(N_l + 3N_y + 4N_x)} \quad (\text{Equation 1})$$

- 139 b. *Trace length*: The trace length of digitised networks and sets within each sample area were
140 assessed using trace length distributions (Andrews et al., 2019; Priest and Hudson, 1981),
141 with the minimum, maximum, and median trace length values used to compare analysis.
- 142 c. *2D fracture intensity*: We compare the intensity of the networks and sets within the
143 network using 2D fracture intensity (Equation 2) (P_{21} ; Dershowitz & Einstein (1988);
144 Rohrbaugh et al. (2002)).

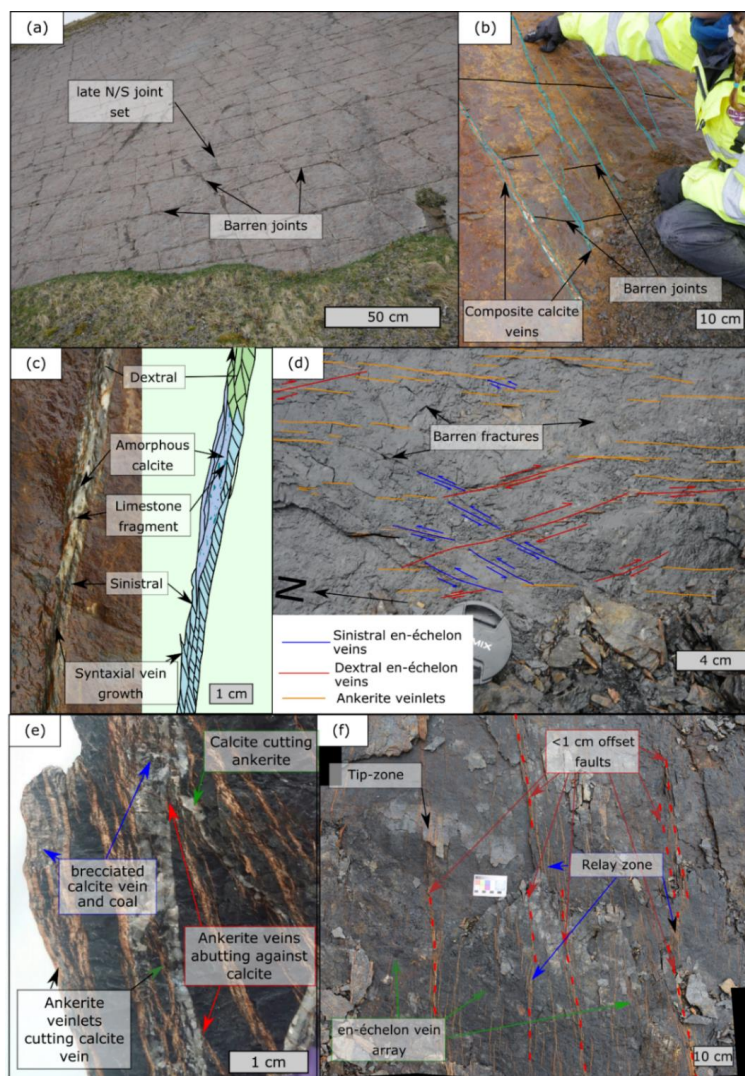
145
$$P_{21} = \frac{\sum tl}{\text{Area}} \quad (\text{Equation 2})$$

146



147 **4. Results**

148 **4.1 General fracture observations**



149 **Figure 2: Typical fracture properties for McDonald Limestone & McDonald Coal:** a) barren joints
150 **observed away from faults across the southerly dipping (c. 40°) McDonald Limestone bedding**
151 **plane;** b) Mineralised N-S trending calcite veins, offsetting abutting E-W ladder joints on the
152 **bedding plane of the McDonald Limestone;** c) annotated field photograph and interpretation of a
153 **multi-phase composite calcite vein exposed in the vicinity to a small offset fault along the McDonald**
154 **Limestone Pavement;** d) bedding plane exposure of mineralised fractures present within the
155 **Muirkirk 6' coal;** e) annotated hand specimen displaying the vein relationships present during the
156 **faulting of the Muirkirk 6' coal;** and f) the larger-scale mineralisation pattern as you move towards
157 **small offset faults in the Muirkirk 6' coal.**



158 Fractures at Spireslack SCM typically occur in two orthogonal directions that vary throughout the site
159 (NS and EW) and can be classified as either joints or shear fractures (often found in the proximity to
160 faults). Away from faults, joints in the McDonald Limestone form two orthogonal barren sets trending
161 roughly NE-SW and NNW-SSE. Orientation of these sets vary, with up to 20° of strike rotation observed
162 throughout the site. Cross cutting relationships show that there are multiple ‘age sets’ (Figure 2a). NE-
163 SW joints formed initially followed by sparsely spaced NE-SW joints then more NE-SW joints, which
164 abut against the pre-existing NNW-SSE trending joints. Finally, a dense network of N-S joints abuts
165 against both sets of E-W trending joints.

166 Calcite mineralisation is observed in the vicinity of, and along, primarily NW trending shear fractures
167 (Figure 2b). Mineralisation occurs as two styles: 1) amorphous, where no growth structures are present
168 and occasional fragments of limestone are observed within the mineralised zone, or 2) with syntaxial
169 growth textures suggesting both sinistral and dextral motion during mineralisation. Along fault planes
170 and within a few meters of faults, composite veins commonly occur, with multiple growth stages and
171 evidence of reactivation (Figure 2c).

172 Fractures in the coal layers are commonly filled with a buff to orange coloured mineralisation, identified
173 in the field as ankerite (iron rich carbonate) (Figure 2d-f). Fractures in coal occur as:

- 174 - *Coal cleats*: Ubiquitous in all coals. Spacing (typically <2 cm) is dependent on bed-thickness,
175 coal quality and the presence of clastic material (e.g. shale partings) (Laubach et al., 1998).
- 176 - *Mineralised shear fractures*: Typically 2 to 15 cm in length, but increase to >1 m long as apparent
177 shear offset increases. Fractures < 15 cm long abut against EW trending cleats, with trace length
178 restricted by cleat spacing. The thickness of planar ankerite veins increases as the length of the
179 fracture.
- 180 - *En-echelon arrays*: En-echelon ankerite veins display both sinistral and dextral motion (Figure
181 2d). Dextral arrays occur both simultaneously with, and later than, sinistral arrays.
- 182 - *Barren shear fractures*: In addition to the cleat network, fractures that abut against all other
183 fractures and are often curved, have trace lengths typically between 5 to 15 cm. These may
184 propagate from the tip of pre-existing mineralised shear fractures (Figure 2d).

185 A complex chronology of fractures is observed in the Muirkirk 6' coal. In Figure 2d dextral offset
186 echelon vein arrays (red) cross cut earlier sinistral sets (blue), with the former abutting against mineralised
187 shear fractures. Barren shear fractures then abut against both sets displaying a curvature indicative of a
188 dextral stress state. Abutting relationships suggest the barren shear fractures likely formed at the same
189 time as the dextral en-echelon vein array; however, they were not connected to a source of mineral rich



190 fluids. In Figure 2e, multiple phases of mineralisation and reactivation of veins can be observed. Veinlets
191 of ankerite both abut against, and cut through the calcite vein associated with a nearby small (<5 cm)
192 offset fault. Brecciation of coal and calcite is also observed, with undisrupted ankerite veinlets cutting
193 through the breccia. This requires a minimum of four stages of mineralisation/deformation:

- 194 1) Ankerite veinlets formed along the NS striking face-cleats.
- 195 2) Faulting leading to the development of coal breccia and calcite veining which either cut across
196 or abut against pre-existing structures.
- 197 3) Brecciation of the calcite vein and coal leading to the development of a chaotic fault breccia.
198 The breccia contains angular clasts of coal and calcite within an amorphous calcite matrix.
- 199 4) Finally, a return to ankerite mineralisation with dextral en-echelon arrays developed alongside
200 barren tip-damage zones.

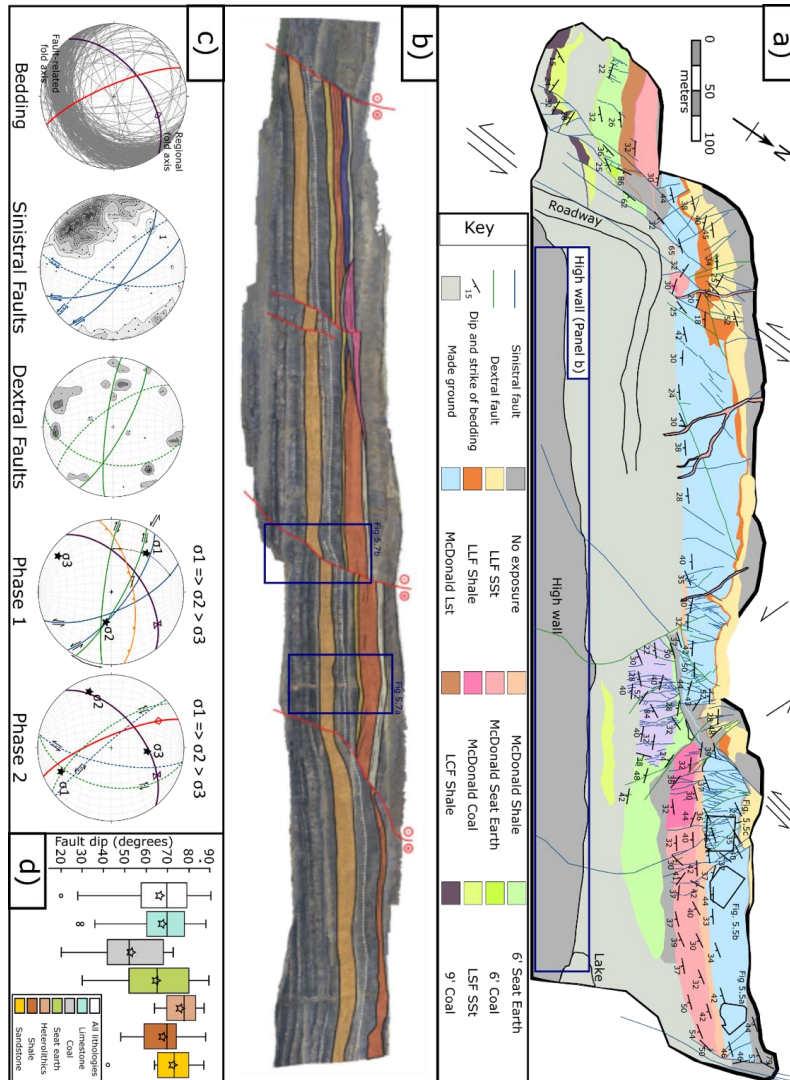
201 These observations suggest that initial deformation and associated mineralisation occurred over a wide
202 zone of en-echelon arrays (Figure 2d), which was strongly influenced by the pre-existing cleat network
203 (Figure 2e). En-echelon arrays then began to interact leading to the development of localised mineralised
204 shear fractures (Figure 2f). As the trace length of the shear fracture increased, so did the thickness of the
205 zone leading to the formation of a dense array of small offset (<1 cm) strands which interacted through
206 the development of relay-zones. A later dextral stress state, demonstrated by reactivated features (Figure
207 2e), lead to another phase of en-echelon veins (Figure 2c), which also locally developed into mineralised
208 shear fractures.

209 The other lithologies display a strongly developed fracture stratigraphy (c.f. Laubach *et al.* (2009)). The
210 McDonald Seat Earth exposed in the western panel (Figure 3a) lacks a well-developed joint pattern.
211 Instead, shear-fractures are observed in relation to small offset strike-slip faults which cut the dip-slope
212 (Figure 4a,b). Fractures are only found in close proximity to fault strands either forming sub-parallel to
213 fault strands in the hanging wall block, or oblique to the fault strands in relay zones and fault tips. These
214 fractures commonly display small sinistral and dextral offsets (mm to cm) and are typically barren,
215 although occasionally showing pyrite along the fracture plane. Sandstones displayed bed-bound joint-sets
216 in a similar manner to the McDonald Limestone. However, there was limited bed-parallel exposure to
217 explore the age and orientation of sets in sandstone lithologies. Seat-earth in the high wall, in contrast to
218 the dip-slope, displays a well-developed bed-bound fracture network. This suggests that mine-related
219 stresses have may have caused deformation of these lithologies and the natural network has been altered
220 by both subsurface and surface mining activities.



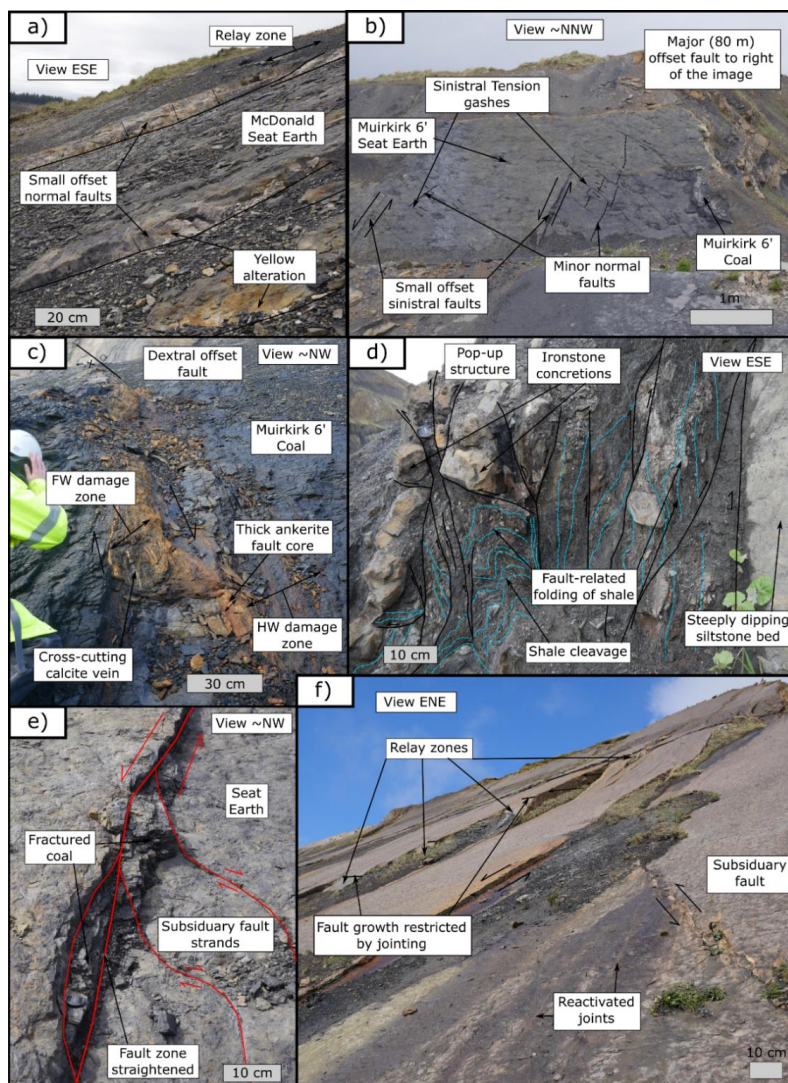
221 **4.2 Fault observations**

222 **4.2.1 Fault kinematics & Self-juxtaposed faults**



223

224 **Figure 3: Geological map of Spireslack SCM: a) Geological map undertaken as part of this study,**
 225 **displaying the locations of the detailed map-view fracture maps shown in Figure 5; b) Annotated**
 226 **photogrammetry of the high wall displaying the key stratigraphic horizons and faults (Ellen et al.,**
 227 **2019); c) Fault kinematics by lithology. Stereographic projections were created using Stereonet**
 228 **10.1 and contours represent 1% area; and d) box and whisker plots for fault dip by lithology.**



229

230 **Figure 4: Characteristic observations of Self Juxtaposed Faults (SJFs): a) Small-offset (c. 15 cm) fault**
231 **strands and relay structures, and b) tension gashes and small offset normal faults exposed within the**
232 **McDonald Seat Earth in seat-earth exposed to the far west of Spireslack SCM; c) symmetric damage**
233 **zone and thick zone of ankerite mineralisation along a c. 40 cm offset dextral offset fault cutting the**
234 **Muirkirk 6' Coal; d) bed-parallel thrusts and folding developed within the shale which underlies the**
235 **McDonald Limestone to the NE of the site; e) the development of small pods of fractured McDonald**
236 **Coal along a small offset sinistral fault exposed to the SW of the site; f) the interaction between faults**
237 **and joints along the southerly dipping bedding plane of the McDonald Limestone.**

238 Several steeply dipping faults with low angle lineations (5° to 30°) were mapped at Spireslack SCM
239 (Figure 3). Fault offset ranges from cm-scale, where displacement is limited to specific lithology (self-
240 juxtaposed), up to the largest offset fault (c. 120 m true offset according to Ellen *et al.* (2016)) which cuts
241 the east of the site. Most faults (75%) belong to a sinistral offset set, which formed simultaneously with



242 ~NE trending dextral faults. Additionally, a later set of sinistral faults with offsets of cm's to m's, and
243 associated dextral faults, offset the earlier faults. Fault strike varies across the main void (Figure 3c), with
244 a N-S trend in the east and west of the site and a NW-SE trend in the centre. Fault dip depends on the
245 lithology cut by the fault. Dips in the McDonald Limestone range from 45° to 88° (mean = 69.1°, n = 47),
246 however, in coal seams fault dips range from 20° to 73° (mean = 49°, n = 24). In the shale interbeds, layer
247 bound bed-parallel thrusts (e.g. 040°/70° SE) with cm to m-scale offsets and associated folding can be
248 picked out where they offset ironstone layers (Figure 4d). The McDonald Seat Earth in the west of the
249 site displays dip-slip slickenfibers (50° to 60°), but only in faults with offset less than 1 m.

250 Self-Juxtaposed Faults, with offset less than 3 m, form either isolated strands (e.g. west of the void), or a
251 network of sinistral and dextral strands (e.g. near the centre of the void) (Figure 3). The internal structure
252 of self-juxtaposed faults depends on the lithology that the fault strand cuts (Figure 4, Table 1). Only large
253 offset fault strands can be traced between beds (e.g. the 5 m offset fault cutting the western panel; Figure
254 3), apart from where large packages of sandstone are found (e.g. the Spireslack Sandstone). For
255 lithologically restricted faults, trace length is typically low and well connected, with strands typically
256 abutting against another fault strand in < 15 m.

257 The majority of faulting at Spireslack SCM fits a sinistral-offset strain-ellipse (Figure 3c). In this model
258 the early dextral faults represent R' Riedel shears, with normal faulting of the McDonald Seat Earth,
259 thrusting in the shale and Riedel shears of the major fault strands which bound the workings developing
260 in the centre of the void. Bedding, which dips towards the south, matches a fold axis of 042°/80° N and
261 is likely to have been developed under the same stress state as the regional Muirkirk syncline. Faulting
262 that cuts the earlier structures (e.g. the oblique sinistral fault and minor dextral fault strands) does not fit
263 within this strain ellipse, and likely formed under a later dextral strain (Figure 3c). In addition to the two
264 phases of strike-slip tectonics, Paleogene dykes are observed exploiting pre-existing N-W trending fault
265 strands. These locally display pods of edge brecciation similar to that developed along faults in limestone,
266 and show dip-slip lineations suggesting there could have been a late stage of normal faulting.

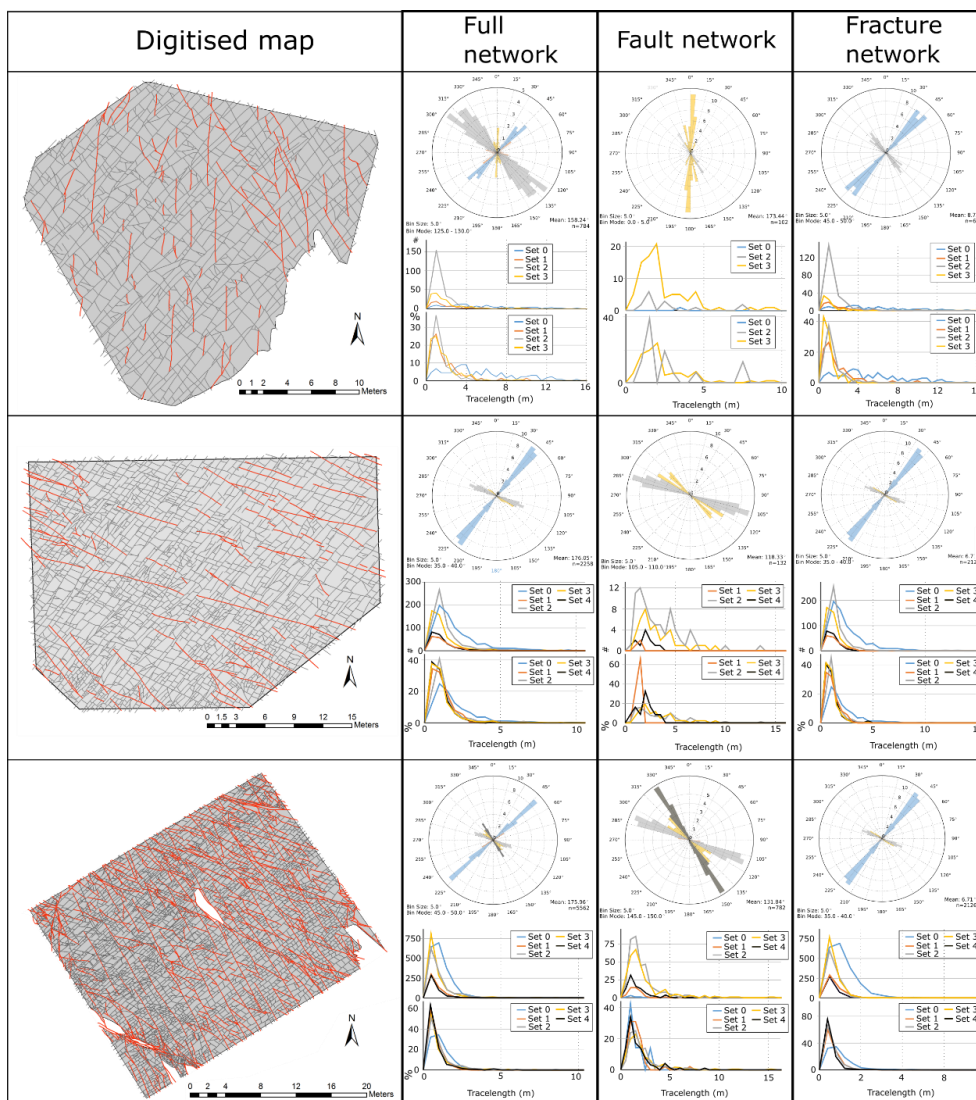


Lithology	Self-juxtaposed fault characteristics
McDonald Seat Earth	Segment linkage, folding, and increased fracturing between strands led to the development of a highly asymmetric damage zone (Figure 4a,f). Faults typically barren, only displaying yellow alteration and occasionally pyrite.
McDonald Limestone	Self-juxtaposed faults, associated relay zones, and nearby N-S trending joint sets, are mineralised (calcite), display high displacement to length ratios (2.4 to 2.8), and show extensive folding of the surrounding lithologies (Figure 5.4f). Strands often abut against favorably orientated pre-existing joints.
Coal	Fault strands are characterised by a fault core comprising of a 5 to 20 cm thick zone of ankerite, with occasional calcite mineralisation, brecciated coal and pyrite (Figure 4c). The fault core is discontinuous along strike, with displacement transferring to other strands after 1 to 5 meters (Figure 2c). The gentle folding of the bed between strands is taken up by a symmetric zone of damage consisting of increased fracturing, en-echelon veining and mineralised shear fractures. The structures represent a continuation of the processes discussed in Section 4.1.1.
Shale	Fault strands are rarely observed. High angle thrusts (40° to 60°) dominate, with bed parallel folding picked out by ironstone concretions (Figure 4d), which themselves can display internal deformation (tension gashes). Near self-juxtaposed faults a cleavage is developed sub-parallel to the fault plane, which combined with slickenfibers on competent bedding planes suggests bed-parallel slip.

267 **Table 1: Self Juxtaposed Fault characteristics.**



268 **4.2.2 Interaction between faults and fractures within the McDonald Limestone**



269

270 **Figure 5: Fracture maps with increasing intensity of faulting: For each digitised map the exported**
 271 **fault (red lines) and fracture (dark grey lines) maps, along with the interpretation areas used for**
 272 **the analysis (light grey) are provided. The orientation data, colour coded by sets, is then provided**
 273 **using length weighted rose diagrams with 5° bin widths. Trace length is presented as trace-length**
 274 **histograms as well as normalised trace-length histograms with bin widths of 0.25 m. Histograms**
 275 **are colour coded to match the sets outlined in the orientation data.**



276 The style of the fault and fracture network in the McDonald Limestone changes across the site (Figure 3)
277 with the chronology and network properties of each sample area described in Table 2. Overall, the
278 network is well connected and dominated by x- and y- nodes, with i-nodes only observed where faults
279 transfer displacement to another strand. As fault intensity increases, the complexity of age relationships
280 in the fault-fracture network increases. Where fault intensity is low and not favourably orientated to
281 reactivate joints (Figure 5), the age relationships match that described in Section 4.2.1. Across all sample
282 areas faults abut against the larger trace-length NE trending set (Figure 5), which are interpreted as
283 forming prior to faulting. When the interaction between faulting and jointing increases, either through an
284 increase in fault intensity or joints being favourably orientated for reactivation, age relationships become
285 complex with new fractures forming concurrently with faulting, probably during stress field rotation. The
286 fact that age relationships vary across the site suggests a highly heterogeneous stress field, which was
287 rotated relative to locally active fault strands. An increase in fault offset also affects the intensity, trace-
288 length and connectivity of the network.



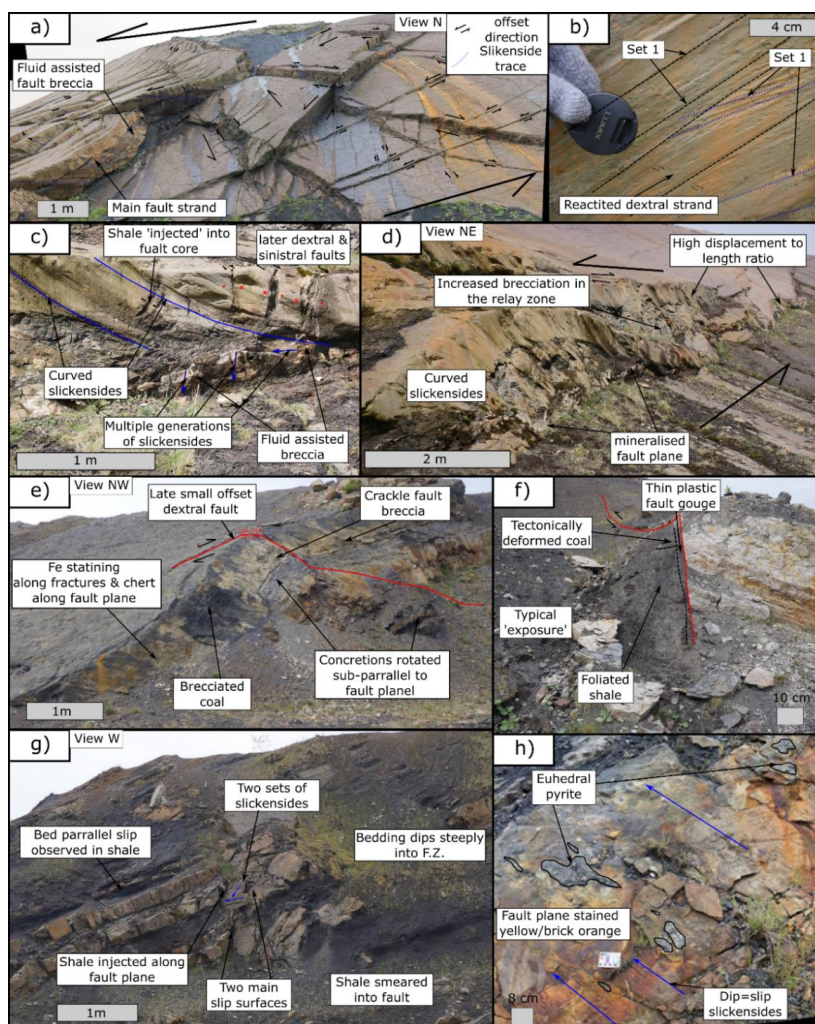
Sample area	Sets & age relations	Trace length & intensity characteristics	Network topology & connectivity
1 Fig. 5a	Joint sets occur as two roughly perpendicular sets, an older 045° trending set and later 145° trending set. Faults are present as a separate NS trending set, which displace both joint sets, typically abut against large trace length NE trending joints, are mineralised and display sinistral syntaxial growth textures (e.g. Figure 2c). In the vicinity, and locally abutting against faults is a final stage of jointing, either associated with initial fault slip or later dextral reactivation.	The NE trending set ranges in has a larger trace length (4.10 ± 3.40 m) compared to the SE trending set (1.30 ± 1.10 m), with the latter typically abutting against the NE trending set. Trace lengths in the NS trending set range from 0.20 to 9.30 m (Median = 1.60 m), and typically abut against the NE trending set. Fault intensity is low (0.4 f/m), with moderate joint density (2.6 f/m) split into 1.3 f/m for the NE set, 1.0 f/m for the SE trending set and 0.3 f/m for obliquely aligned features.	The connectivity of the full network is high (Pc = 0.99) and is dominated by y nodes (76%), with X-nodes representing 23% of nodes. Field observations suggest the majority of x-nodes mapped on the drone map represent two y-nodes separated by <5 cm. The fault network is dominated by l nodes (90%) and is poorly connected (Pc = 24%). The joint network is dominated by y-nodes and has a connectivity of Pc = 95%.
2 Fig. 5b	Dominated by barren joints, with faults displaying a NW trend, which reactivate appropriately orientated joints and abut against NE trending joints. The age relationships are complex and show multiple generations of joints, typically orientated in a NE or NW trend, however, many joints are observed which do not fit these sets.	Faulting is slightly higher intensity than SA1 (0.5 f/m), with fault trace length varying between 0.20 and 13.20 m (median 1.20 m). Small trace length faults are found oblique to the main strand (e.g. northerly trending faults median trace length = 0.80 m). Joint intensity is 3.1 f/m with the majority of fractures belong to the NE (1.7 f/m) or NW (0.7 f/m) trending sets. Fractures off this trend typically have smaller tl (Median = 0.60 to 0.70 m) compared to the NE (median = 1.30 m) and NW (median = 1.00 m) sets.	The connectivity of the full network is high (Pc = 0.99) and is dominated by y nodes (88%). The fault network is dominated by l nodes (89%) and is poorly connected (Pc = 28%). The joint network is dominated by y-nodes and has a connectivity of Pc = 90%.
3 Fig. 5c	The complexity of joints varies considerably throughout SA3. Some areas display a simple relationship with an early ENE trending set and later NNW trending set, however, other areas display fracture corridors, which are aligned at a similar orientation to faulting, and which display multiple generations of joint formation. Faulting occurs as two sets, trending NNW, and NW. Faults typically abut against ENE trending joints, and locally cause the formation of new joints and rotation of pre-existing features.	Faulting intensity increases considerably in SA3 (1.9 f/m), with fault trace length ranging from 0.10 to 15.30 m (median = 1.40 m). The majority of faults trend between 125° and 155° (0.16 f/m) and display a higher median trace length (1.40 m) compared to other faults (1.10 m). Joint trace length is smaller in SA3 (0.50 m) compared to other sample areas (Median tl = 1.00 m and 0.80 m). Although most joint trend is NE (2.4 f/m) the NW trending set displays a wide range in orientation (125° to 155°) and 17% of joints are off axis from these trends. NE joints display a larger trace length, ranging from 0.00 to 5.50 m (median = 0.70 m) compared to other orientations (median = 0.40 m).	The connectivity of the full network is high (Pc = 0.99) and is dominated by y nodes (93%). The fault network is dominated by both l- (55%) and y-nodes (45%) and is moderately connected (Pc = 71%). The joint network is dominated by both i- and y-nodes and has a connectivity of Pc = 77%.

289

290 **Table 2: Network characteristics for the sample areas outlined in Figure 5**



291 **4.2.3 Large offset faults**



292

293 **Figure 6: Large offset fault characteristics:** a) complex fault mesh consisting of multiple strands of
294 sinistral and dextral strike slip fault planes (offset marked with arrows) picked out by shallow
295 striations and the offset of the McDonald Limestone bedding plane; b) field photograph of a ~3 m
296 offset fault strand within the complex mesh which displays multiple generations of fault striations,
297 with local dextral reactivation separating striations belonging to set 2; c) fault architecture and d)
298 view along strike of a 3 to 5 m offset fault strand exposed along the southerly dipping bedding dip-
299 pose; fault architecture of the same 5 m offset fault cutting e) lithologies surrounding the McDonald
300 Seat Earth, and g) interbedded sandstones, siltstones and shales of the Lower Limestone Coal
301 Formation; f) primary slip plane of the ~80 m offset fault which cuts the west of the site; and h)
302 shallowly dipping, sinistral dip-slip fault plane within a ~2 m thick sandstone bed of the Limestone
303 Coal Formation.



304 Faults that offset multiple lithologies (i.e. non self-juxtaposed) have a complex deformation style (Figure
305 6). Fault dips still vary depending on lithology, with steeper dips observed in competent lithologies for
306 the same fault. For example, a 4 m offset fault changes orientation from 135°/85° NE in the McDonald
307 Limestone to 110°/72° N in the McDonald Seat Earth. This change in orientation causes bed rotation and
308 the development of lenses, particularly in sandstones and seat-earths. Examples of larger-offset faults are
309 provided below, with the complexity of faulting depending on the lithologies cut by the fault (Figure 6)
310 and the plane of observation (i.e. map (Figure 3) vs high wall (Figure 7)).

311 *Example 1: Fault meshes in the McDonald Limestone and surrounding lithologies*

312 Faults cutting the McDonald Limestone with less than 3 m offset lead to the development of fault meshes
313 (Figure 6a). Rotation of bedding is accommodated along several fault-strands accompanied by the
314 development of tension gashes. The thickness of individual fault cores is low (<5 cm, Figure 6a,b), and
315 does not increase with displacement. Fault cores are mineralised, with local development of matrix-
316 supported breccias containing angular limestone clasts and clasts of re-worked calcite. These textures,
317 along with the development of Mode 1 fractures that offset previous slickenfibers (Figure 6c),
318 demonstrate fault reactivation. Multiple generations of slickenfibers are developed whose dip shallows
319 from the top to the base of the bed (Figure 6c, insert), providing further evidence of block rotation within
320 the fault zone. Folding and bed parallel deformation of the under- and over-lying shale helped
321 accommodate this rotation.

322 *Example 2: Dip-slip faulting of sandstones and seat earths*

323 3D exposures of faults cutting sandstone are rarely observed, however, in the center of the void there a 3
324 to 5 m offset fault cuts decimetre thick seat-earth and sandstones of the Limestone Coal Formation (Figure
325 3). The fault-plane is low-angled (100°/40° S) and displays dip-slip (40° to 55°) lineations. The fault plane
326 is altered to a brick-orange colour (Figure 6). Pyrite is locally preserved within corrugations along the
327 fault plane and consists of <4 cm euhedral crystals (usually <0.5 cm). The alteration and pyrite
328 preservation suggests sulphur-rich fluids migrated along the fault zone, and pods of crystal growth
329 developing elongated to the slip-vector suggesting this was syn-kinematic. Where coal is observed above
330 seat-earth (Figure 4e), brecciation of coal, thin zones of friable coal develop and cleats are rotated relative
331 to the orientation of the fault plane.



332 Example 3: ~5 m offset fault cutting interbedded lithologies from the Lower Limestone Formation and
333 Limestone Coal Formation

334 A ~5 m offset, sinistral fault is observed cutting limestones and sandstones of the Lower Limestone
335 Formation and the McDonald Seat-Earth to the west of the void (Figure 3). In the McDonald Seat Earth
336 (Figure 6b) fault dip changes from ~60° near the base of the outcrop to 007°/79° NE near the top and low
337 angle lineations (e.g. 20°/107°) and offset markers indicate a sinistral offset. The main fault plane is cut
338 by several later barren fractures (e.g. 116°/74° N and 292°/71° NE), which occasionally show cm-scale
339 sinistral offset (18°/019°). Brecciated McDonald coal is found within undulations on the fault plane. In
340 the underlying shale, several iron concretions (<10 cm) have been locally rotated and sheared in response to motion along the
341 fault. An asymmetric damage zone is developed, with minimal deformation of the footwall and a 20 to 30
342 cm wide zone of higher fracture intensity developing in the hanging wall. Bedding in the seat earth away
343 from the the fault displays gentle (2-5m wavelength), low amplitude (~50 cm) folding with wavelength
344 decreasing towards the fault.

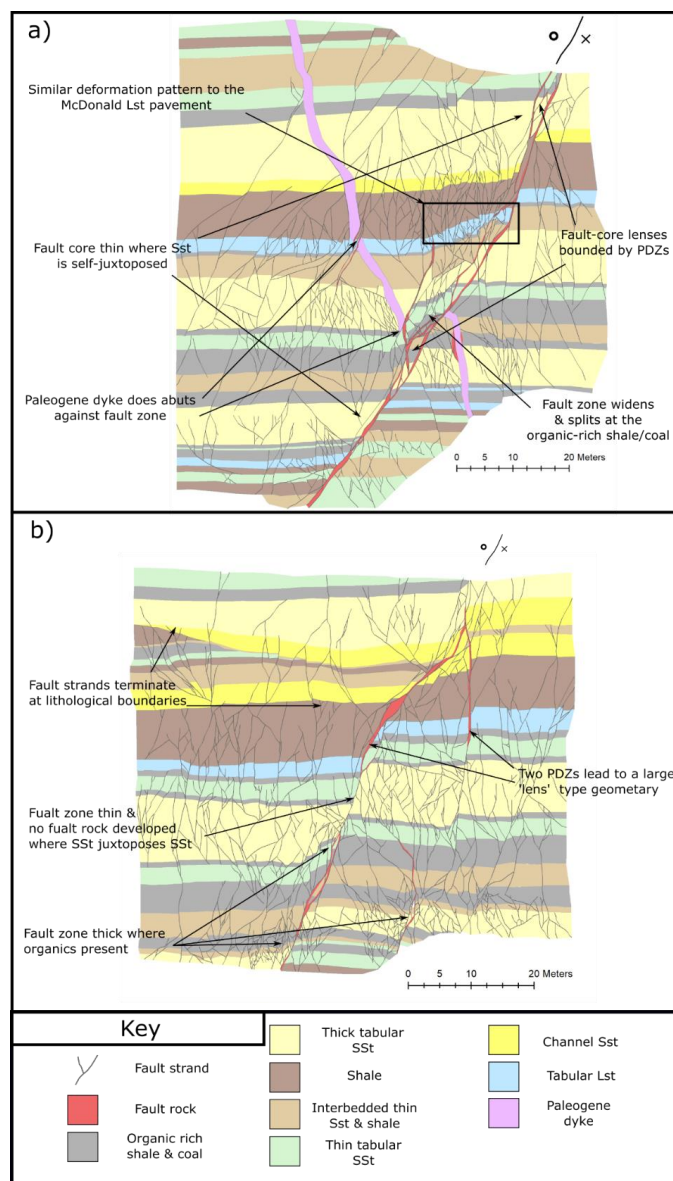
345 In the underlying Lower Limestone Formation, the same fault develops a complex, 2 to 3 m thick,
346 mineralised fault zone (Figure 6c). The fault core is characterised by two mineralised slip surfaces
347 (216°/60° W & 261°/68° NW), each with shallow (10°/080°), moderate (25°/050°) and steeply (68°/083°)
348 dipping sets of slickenfibers developed. It is unclear which order these developed, and all apparently
349 display sinistral offset markers. Along the fault surface (015°/88° E), a ~5 cm thick pod of matrix
350 supported brecciated limestone is present in the hanging wall. Shale appears to have been locally injected
351 into fractures that had already been mineralised with calcite. To the north of the fault, the interbedded
352 sandstones, limestones, and shale dip steeply into the fault zone, reaching dips which match that of the
353 fault plane (60° to 70°). In contrast, bedding to the south displays only low amplitude folding (015°/56°
354 N; 043°/56° N).

355 Example 4: 80 to 100 m offset fault cutting the full sequence

356 The internal structure of the 80 to 100 m offset fault that cuts the west of the main void is only observed
357 at a single location (Figure 6e). The footwall comprises 6' Seat Earth that has been highly fractured,
358 juxtaposed against highly altered coal and folded shale with a steeply dipping cleavage. The fault core is
359 comprised of a thin (<5 cm), clay rich zone of plastic fault gouge containing <2 mm clasts of sandstone
360 and organic fragments. The altered coal has lost its cleat network and is noticeably harder than its
361 unaltered equivalent, creating a spark when struck with a geological hammer. This increase in coal rank
362 is potentially due to shear-heating (c.f. Fowler and Gayer, 1999; Li, 2001). Shear fractures in the
363 surrounding seat earth are often stratabound and increase in intensity towards minor-slip zones and the
364 fault core.



365 *Example 6: Fault strands cutting the high wall*



366

367 **Figure 7: Digitised fault strands of sinistral faults cutting the Limestone Coal Formation exposed**
 368 **along the high wall: a) sinistral fault which displays between 2 and 5 m of throw and has been cut**
 369 **by a later Paleogene dyke which is not observed with the main PDZ; b) sinistral fault with displays**
 370 **between 2 and 8 m throw along two PDZs.**



371 Fault strands cutting the high wall (Figure 7) appear to show a simpler geometry to those observed on the
372 dip slope (Figure 6). It should be noted that because of the predominant strike-slip kinematics significant
373 out of plane displacement exists, so visible offsets represent an underestimate of true displacement. The
374 majority of throw is taken up by a small number of fault strands, particularly when faults cut channelised
375 sandstones and limestones. Individual fault strands are thin and form an interconnected network of self-
376 juxtaposed faults. Fault core thickness is typically below the width of a pixel on the orthorectified
377 photographs (~5 cm), however, on the major faults the fault-rock thickness can be measured, although
378 the rock type not quantified. The thickness varies considerably down-dip (<1.4 m), and while a continuous
379 strand is observed in Figure 7a, in Figure 7b no fault rock is observed where the thick sandstone bed is
380 self-juxtaposed.

381 The deformation style in the high wall varies depending on the lithological juxtaposition, with the
382 proportion of sandstone in the faulted section controlling whether fault-core lenses are developed. For
383 example, in both panels of Figure 7 fault-bounded lenses are seen in the lower third of the high wall.
384 Faults are steep (apparent dip ~70° to 80°) with displacement taken up along a single fault strand, and
385 damage zone evolution is low in areas where thick sandstone units are juxtaposed. However, where
386 interbedded units are juxtaposed against each other the fault zone widens to 4 m in Figure 7a and 4.5 to
387 6 m in Figure 7b. Within these zones beds of competent lithology are rotated away from the main fault
388 zone and subsidiary antithetic fault strands develop which abut against the main strand. Small offset faults
389 are more abundant in the thick tabular sandstone, interbedded and shale units, with fault stands abutting
390 and branching at lithologically controlled mechanical boundaries.

391 **5. Discussion**

392 **5.1 The role of lithology on faulting style: self-juxtaposed vs non self-juxtaposed faulting**

393 The observations at Spireslack SCM suggest that faults initiated both in the competent lithologies
394 (sandstone, seat-earth and limestones) and the coals (Figures 3, 4). The properties of the faults (trace
395 length, connectivity, D-L ratio and fault-rock development) depend on the lithology being cut, and the
396 degree of non-self-juxtaposition. This is similar to observations of the growth of normal faults in
397 interbedded limestones and marls (Ferrill et al., 2017), basalts (Ellen 2011), as well as 2D and 3D
398 numerical modelling (Schöpfer et al., 2007, 2016). Self-juxtaposed faults developed in all the competent
399 layers at the same time and initially grew as isolated strands, before interacting with other strands from
400 the same unit. This behaviour matches established models for fault growth (Fossen and Rotevatn, 2016;
401 Walsh et al., 2002; Wibberley et al., 2008).



402 However, large offset faults which breach more than a single lithology are strongly affected by the
403 presence and behaviour of shale interbeds. Shale in the sequence behaves in a ductile manner with folds
404 and cleavage developing (Figure 4d), and enables bed-parallel slip. In Figure 6g, shale is squeezed into
405 pre-existing mineralised fractures, indicating the highly ductile nature of shale during faulting. The
406 ductility of shale can be affected by many factors including lithology, mineral composition, organic
407 carbon content, diagenesis, and thermal maturity (Wang and Gale, 2009). Burial depth is a major
408 controlling factor for many of these properties and it is important to consider both the current and past
409 burial depth (Yuan et al., 2017). As shale is buried and compressive stresses increases, the ratio of pre-
410 consolidation stress and compaction-related stresses control the behaviour of shales and mud rocks (Yuan
411 et al., 2017; Nygård et al., 2006). As a general rule, shales are ductile during burial, and brittle during
412 exhumation where they experience stresses below the maximum stress they have encountered. While
413 estimates vary across the Midland Valley, it is suggested the Limestone Coal Formation has a maximum
414 burial depth of <3,000 m at around c. 60 Ma (Monaghan, 2014). Ductile behaviour of the shales at the
415 time of faulting suggests that faulting was active during burial, rather than uplift. This will have enabled
416 faults to initiate as isolated strands in competent lithologies. When faults accumulated enough
417 displacement to cut multiple lithologies, shales accommodated the rotation of bedding, leading to rotated
418 blocks and multiple generations of curved slickensides.

419 Self-juxtaposed faults coal remained relatively undeformed, or developed a thin zone of ankerite
420 mineralisation. This differs from published examples in, where tectonically deformed coals in the form
421 of soft-coal bands are often associated with normal faults (Godyń, 2016; Ju et al., 2012; Li et al., 2018),
422 or bed-parallel slip in compressive environments (Frodsham and Gayer, 1999; Li, 2001). Soft coal bands
423 often display a range of brittle and ductile features, for example S-C type cleavages, minor thrusts and
424 folding (Li, 2001), all of which act to degrade the quality of the coal. Archival photographs of the far
425 east of the site show that soft-coal bands were also not developed where coal was extracted from an area
426 where bedding steepened to $\sim 70^\circ$ (Ellen et al., 2016; Leslie et al., 2016).

427 The fault core of the large offset faults often contain pods of coal present as un-mineralised chaotic fault
428 breccia (Figure 6e). These deposits form in asperities along the fault zone, which get cut as the fault
429 straightens. Asperities, formed by corrugations along the fault zone, have previously been identified both
430 in the field (Sagy et al., 2007; Wright and Turner, 2006) and from seismic data (e.g. Lohr *et al.* (2008)).
431 Asperities typically form aligned parallel to fault slip (Hancock and Barka, 1987), which is also observed
432 in fault zones at Spireslack SCM. The behaviour of coal in the larger faults (Figure 6) differs from small
433 offset faults (Figure 4) in that no mineralisation is observed. Where coal was observed overlying seat-
434 earth (Figure 4e), coal was rotated, brecciated and thin zones of friable coal developed, suggesting that
435 coal becomes entrained into the fault core as a rotated block, similar to a fault-core lenses (Gabrielsen et



436 al., 2016). This suggests that while self-juxtaposed faults can be used to understand fault growth up to a
437 certain point, once multiple lithologies are cut the processes change such that self-juxtaposed faults are
438 not representative of large offset faults (c.f. Ellen, 2011).

439 **5.2 Jointing and the effect of pre-existing weaknesses on the deformation style and fault growth**

440 The mechanically stratified succession at Spireslack SCM has led to the development of a fracture
441 stratigraphy (Laubach et al., 2009). Orthogonal joint sets are developed in the MacDonald Limestone
442 (Figure 2a), as cleats in the MacDonald coal (Figure 2d) and bed-bound joints within the sandstone layers.
443 While only two orientation sets are observed within the MacDonald limestone, abutting relationships
444 show these formed as at least 4 ‘age sets’. Similar observations reported for other sites (Peacock et al.,
445 2018; Sanderson, 2015) confirm that fractures in the same orientation, did in fact grow in response to
446 separate deformation events. Another way in which multiple age sets can develop is where the
447 intermediate (σ_2) and minimum (σ_3) principal stresses are nearly identical, and can therefore easily switch
448 between each other (Caputo, 1995; Caputo and Hancock, 1998). The ratio of principal stresses changes
449 the mechanical response of the layer (Healy et al., 2006; Moir, 2010; Moir et al., 2010)), with the dip and
450 dilatancy of fractures varying depending on the difference between (σ_2) and (σ_3) (Chang and Haimson,
451 2000; Haimson and Chang, 2000).

452 The joints at Spireslack SCM formed both prior to and associated with faulting: the sparsely spaced joint
453 set likely forming in response to far-field stress fields during burial, and later sets related to the early
454 stages of faulting and folding associated with the Muirkirk Syncline. This folding, and later faulting is
455 attributed to mid-to late Carboniferous sinistral transpression (Leslie et al., 2016). A late-stage dextral
456 event locally reactivates these structures, reactivates cleats within the coal (Figure 2 d, e, f), and locally
457 causes kink-bands to develop. This dextral strain was not identified in the work of Leslie *et al.* (2016).
458 and could be correlative to Upper Carboniferous deformation to the east of the MVS (Underhill et al.,
459 2008). Paleogene dykes, intruded along pre-existing NE to N trending faults, display a minor amount of
460 reactivation, with brecciation and dip-slip lineations developing along the margins. This suggests that late
461 stage extension, orientated to enable the reactivation of NE trending structures occurred since the
462 Paleogene, possibly linked to isostatic rebound or the opening of the North Sea or Irish Sea.

463 The presence of joints in the McDonald Limestone, and cleats within the Muirkirk 6’ Coal influence the
464 internal structure and fault growth in these lithologies (Figure 4, 6). In both lithologies multiple sets of
465 pre-existing weaknesses existed at the time of faulting, however, it was only those orientated roughly
466 orthogonal to fault trend which caused fault strands to terminate (Figure 4). Coal cleats in the Muirkirk
467 6’ Coal show evidence of reactivation (forming mineralised shear fractures and en-echelon arrays), and
468 may act to restrict the growth of these features. Although small-offset fault strands display evidence of



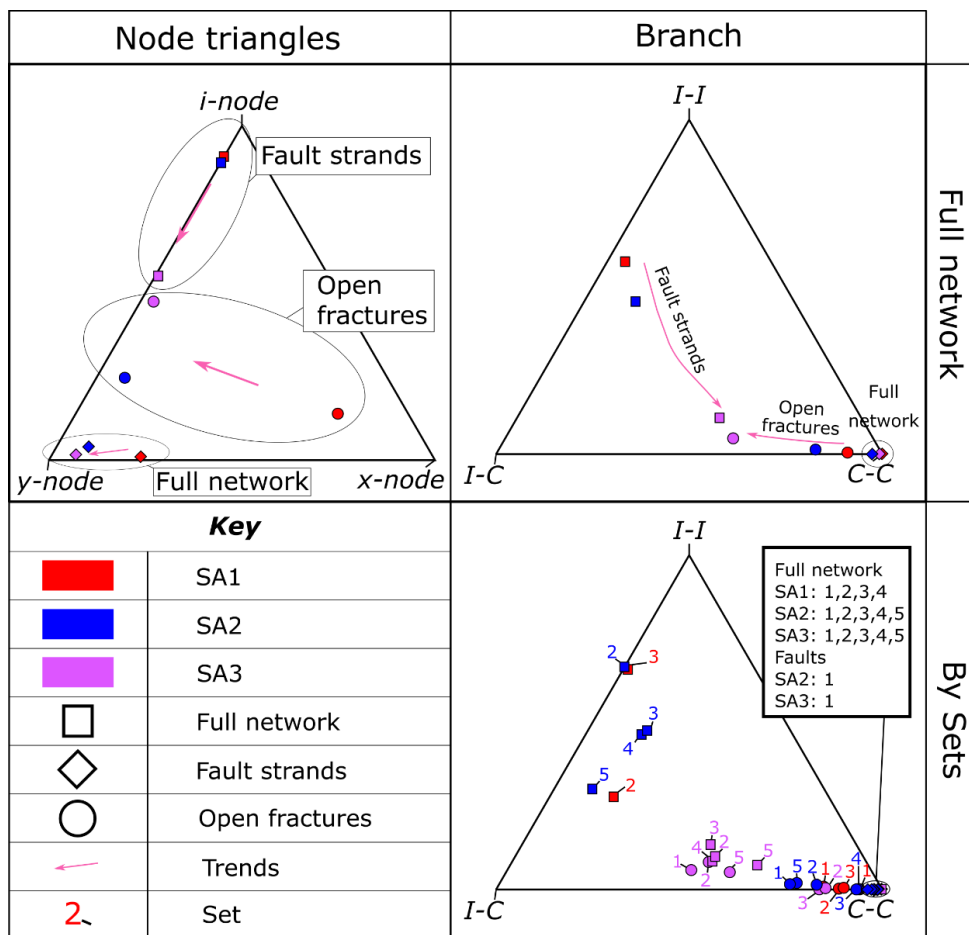
469 reactivation (e.g. brecciated coal, calcite and ankerite), further displacement is often taken up by the
470 formation of new shear fractures. Mineralisation of the cleats causes the strain-hardening of the coal with
471 pre-existing weaknesses (cleats) becoming mineralised strength inclusions. During the dextral
472 deformation stage new mineralised fractures formed, and tip-damage zones developed from the end of
473 shear fractures that had developed during the sinistral phase.

474 While joint sets in the McDonald Limestone may become rotated close to fault strands, no increase in
475 fracture intensity is observed and a typical core-damage zone structure is not developed (e.g. Caine *et al.*
476 (1996); Gudmundsson *et al.* (2010); Bense *et al.* (2013)). Mineralisation (primarily calcite) increases
477 towards the fault core, with fault cores in the McDonald limestone comprising of multiple generation of
478 slickensides, mineralisation and calcite matrix chaotic fault breccias (Figure 6a, c). While some rotation
479 of individual joints occurs towards the east of the site, the majority of joints remain planar and instead
480 acted as planes of weaknesses which became reactivated to accommodate fault slip. The rotation of joint
481 strike is in part related to the bulk rotation of competent beds along shale inter-beds into fault zones which
482 is observed both along the dip-slope and high wall. In Figure 5, the folding of the McDonald Limestone
483 can lead to previously mis-oriented joints becoming more favourably orientated to reactivation

484 Displacement on large offset faults, such as those observed in the high wall, is typically localised onto a
485 small number of principal displacement zones (Figure 7). This indicates that while jointing strongly
486 impacts early fault parameters, once a fault reaches a certain displacement, small-scale features such as
487 joints have only a minor effect on fault growth. The effect of joints on the early growth characteristics of
488 faults is discussed by Wilkins *et al.* (2001), who found faulted joints to develop little fault rock, and to
489 have considerably smaller displacement/length ratios that would be expected for faults which do not cut
490 jointed lithologies. Pre-existing joint-sets restrict fault-growth for self-juxtaposed faults through the
491 formation of faulted joints (Peacock, 2001; Soden *et al.*, 2014; Wilkins *et al.*, 2001), with lithology
492 becoming the major control once faults breach multiple layers (Nicol *et al.*, 1996; Soliva and Benedicto,
493 2005; Wilkins and Gross, 2002). This behaviour is not observed in the McDonald Seat Earth, where
494 jointing is not present. Instead fault strands grow as single strands, which interact with other strands to
495 form tip-damage zones and relay zones where displacement transfers between fault strands (Fossen and
496 Rotevatn, 2016).



497 **5.3 Effect on flow pathways**



498

499 **Figure 8: Network topology data.** Node and branch triangle (after Sanderson & Nixon (2015)) are
 500 presented for the full-network, mineralised fault strands, and open joints, for each of the three
 501 sample areas shown in Figure 5. Branch data is then presented by sets, as outlined in figure 5, to
 502 investigate the directionality of network connectivity.



		Network parameter	Sample area		
			SA1	SA2	SA3
a) Combined network		#lines	784	2258	5562
		D (F/m ²)	3.1	3.5	5.9
		Pc	1.00	0.99	0.96
	TI (m)	Min	0.09	0.02	0.04
		Max	14.71	13.16	15.33
Median		1.12	0.90	0.51	
b) Fault network		#lines	102	132	782
		D (F/m ²)	0.4	0.5	1.9
		Pc	0.24	0.28	0.71
	TI (m)	Min	0.22	0.21	0.10
		Max	9.33	13.16	15.33
Median		1.62	2.34	1.36	
c) Joint network		#lines	682	2126	4778
		D (F/m ²)	2.6	3.1	3.9
		Pc	0.96	0.90	0.77
	TI (m)	Min	0.09	0.02	0.04
		Max	14.71	10.33	5.49
Median		1.53	0.86	0.46	

503 **Table 3: Overview of network properties for: a) the combined fault and fracture network; b) the**
 504 **mineralised fault network; and c) the joint network which does not display mineralisation or**
 505 **reactivation during faulting.**

506 Mineralisation along fault planes within coal (Figure 4), limestone (Figure 4 & 6), sandstone (Figure 6),
 507 and to a lesser extent seat-earth (Figure 4 & 6), locally provides evidence of flow within the structures.
 508 Fault-related veins display one or more crack-seal events (Figure 2c) indicating along-fault flow was
 509 related to fault assisted opening of dilatational zones leading to the connection of pre-existing fractures
 510 (Ferrill and Morris, 2003; Laubach et al., 2009; Ferrill et al., 2014). The multiple events suggest pathways
 511 only remained open for a small amount of time and probably closed following fault slip (c.f. Sibson 1990,
 512 1992). Faults in the McDonald Limestone behave in a similar way to other faults in carbonates with
 513 primary slip surfaces becoming sealed following slip (e.g. Billi *et al.* (2003)).

514 Fault-related mineralisation in both limestones and coals would act to reduce connectivity, and hence
 515 permeability, of the network (Figure 8). At the time of faulting, the majority of the network had been
 516 formed, however, only joints/cleats orientated favourably for reactivation became mineralised. Following
 517 mineralisation, these fractures became sealed and closed to future fluid flow. During faulting, the
 518 connectivity of the network on the McDonald Limestone bedding plane varies depending on the intensity
 519 of faulting (Table 3). Fault-assisted fluid flow in areas of low fault intensity (0.4 f/m²; Figure 5) was
 520 primarily confined to a sparse network of partially connected NS trending, poorly connected (Pc = 0.24)
 521 fault strands. Where faulting of a similar intensity (0.5 f/m) is orientated favourably to reactivate joints



522 (SA2), the connectivity remains low ($P_c = 0.28$), however, fault trace length is greater due to the
523 orientation and spacing of pre-existing joints. When faulting intensity is high (1.9 f/m), the connectivity
524 of faults is high ($P_c = 0.71$), and both sets of joints become reactivated. Because multiple sets of joints
525 may restrict the growth of faults, trace length of individual fault strands is low and strain is taken up by
526 many small offset faults.

527 Faulting caused the development of several new joints, with joint intensity increasing from 2.6 in SA1
528 where limited shear fractures are observed, 3.9 f/m where fault intensity is high. The joint network initially
529 remains well connected ($P_c = 0.96$), however, as joints become reactivated connectivity drops to $P_c =$
530 0.90. In SA3, where fault intensity has increased to 1.9 f/m, the connectivity of the joint network drops
531 to $P_c 0.77$. It is also important to consider the orientation of the feature when considering fluid-flow
532 properties of the network. For example, while faults typically have a low to medium number of
533 connections per branch, those orientated between 060° and 100° plot close to the C-C vertex of the branch
534 triangle (Figure 8). This is also observed for joint sets, with those trending to the NW being the most
535 connected.

536 The evidence of transient fluid flow in both the McDonald Limestone and Muirkirk 6' Coal highlights
537 the importance of understanding the evolution of a fault and fracture network when assessing the
538 geological and fluid-flow history of a particular site. If fracture data were collected using the high-
539 resolution imagery alone, and not combined with field evidence, all fractures might be assumed to have
540 been open to flow. This would lead to a significant over-estimation of the permeability of the network.
541 For example, in SA3 the connectivity of all lineaments is $P_c = 0.96$, however, when only joints which
542 have not been reactivated by faulting are considered, this drops to $P_c = 0.77$. In this case the trace length,
543 which represents one of the most important parameters in fracture modelling (Lei et al., 2017; Min et al.,
544 2004) would also be overestimated, with mineralised fault strands displaying a larger median trace length
545 of 1.36 m. The presence of mineralisation only within particularly orientated joint or cleat sets also
546 highlights the importance of stress state on hydraulic properties of fractures (Cherubini et al., 2014).
547 While no data exist to quantify the magnitude of modern day stresses in Scotland (Comerford et al., 2018),
548 the stress orientations have been suggest as roughly EW extension (Baptie, 2010), and a northerly trending
549 maximum compressive stress (Heidbach et al., 2008). This stress orientation would tend to reduce the
550 aperture of large trace length ENE to NE trending joint sets, further reducing the modern-day connectivity
551 of the network.



552 5.4 Implications for growth of strike slip faults

553 While the role of mechanical stratigraphy on normal faults has received considerable attention, relatively
554 few studies have focused on the effect on the development strike-slip faults (Gross et al., 1997; Nemser
555 and Cowan, 2009; Sylvester, 1988). With the abundance of small-offset strike-slip faults in transtensional
556 basins, it is of increasing importance to be able to predict the behaviour of such structures for hydrocarbon
557 extraction (e.g. Gamson *et al.* (1993); Shuichang *et al.* (2009)), shallow geothermal projects (e.g.
558 Malolepszy (2003)), carbon capture and storage (Solomon, 2007), and geotechnical engineering
559 (Donnelly, 2006).

560 The amount of strike-slip on these faults is not quantified: the irregularity in the slip vectors makes
561 calculations of total slip based on dip slip and slickenlines unreliable. However, the total slip is likely to
562 be substantially greater than the observed dip-slip with slickenlines between 5 and 30 degrees rake, the
563 total slip will be 2 to 11.5 times the dip-slip distance. The total thickness of all fault strands is low, with
564 a maximum thickness of fault rock of 1.4 m (including fault-core lenses), and typically <30 cm. This
565 value is low even for scaling of dip-slip displacement and thickness. This implies that the fault zone
566 thickness has not grown as a function of the total slip.

567 The orientation of the pre-existing weaknesses and bedding with respect to the fault growth geometry is
568 different for strike slip faults than normal faults. We find the growth of mineralised shear fractures and
569 self-juxtaposed faults in coal to be retarded by the pre-existing joint network (Figure 2 & 4). Similarly,
570 in Figure 5 favourably orientated joints either retarded the growth of self-juxtaposed faults, or are
571 reactivated as shear fractures in the McDonald Limestone. The orientation of features that are orthogonal
572 to propagation direction (e.g. NE joints cutting the McDonald Limestone), will cause a mechanical
573 barrier. However, joints that are favourably orientated will be re-activated. Similar differences in
574 mechanical response relative to an applied stress has been observed in rock deformation experiments for
575 planar weaknesses (e.g. mud laminations (Whittles et al., 2002)) and cleats (Li et al., 2016). Unlike normal
576 faults, where fault strands will step between joints in different beds (Wilkins et al., 2001; Wilkins and
577 Gross, 2002), in strike slip faults self-juxtaposed faults will step in bedding-parallel view. The local
578 orientation of joint sets, which is altered by the folding of competent layers (Figure 3) leads to the complex
579 interaction of faults and joints observed at Spireslack SCM (Figure 5). In non-self-juxtaposed faults
580 (Figures 6 & 7), it is instead primarily bedding which cause the termination of fault strands. Although
581 this is similar to normal faults in mechanically layered sequences (Ferrill et al., 2017), the effect is less
582 than would be expected and single through-going footwall strands are often observed. This suggests that
583 the orientation of bedding and bed-perpendicular will have a significantly significant impact in the growth
584 of strike slip faults than dip-slip faults.



585 **6. Conclusions**

586 The exceptional exposures of the Limestone Coal Formation exposed at Spireslack SCM enabled the
587 effect of lithology and pre-existing structures on the internal structure, fluid flow properties, and growth
588 faults to be investigated. We find that the internal structure of fault strands is strongly affected by: a) the
589 lithology that was faulted; b) whether multiple lithologies are cut by the fault or not; c) the presence and
590 behaviour of shale interbeds, and; d) the presence and orientation of pre-existing fractures. The geological
591 evolution of Spireslack SCM displays a complex relationship of folding, brittle deformation and stages
592 of mineralisation.

593 Faults in the McDonald Limestone and Muirkirk 6' Coal are strongly affected by the presence of the pre-
594 existing joint and cleat network. In both cases, this causes the restriction of fault growth, with individual
595 strands abutting against favourably orientated structures. The mineralisation of the cleat network in the
596 Muirkirk 6' Coal led to an increase in the strength of the coal seam, with later reactivation concentrated
597 at the tips of mineralised cleats. This is not observed in the McDonald Limestone, but the strength
598 difference between the vein fill and the host rock is less. In both units, because fault planes become
599 mineralised the permeability of the rock mass decreases as fault intensity increases. Our work
600 demonstrates the importance of considering not just the lithologies being faulted, but also whether pre-
601 existing weaknesses are present. Where pre-existing weaknesses are present, fault-growth will be
602 restricted and the connectivity of a network can drastically change through time following mineralisation
603 and/or changes in stress directions/folding.

604 **Acknowledgements**

605 This work was funded through BJA PhD studentship, supported by the Environmental and Physical
606 Sciences Research Council (EPSRC, award number EP/L016680/1). LMCK is supported by a University
607 of Strathclyde Environmental and Physical Science Research Council (EPSRC) Doctoral Training
608 Partnership (DTP) award (award reference 1904102). We would like to thank Dave Healy for the use of
609 the high-resolution photomontage of the McDonald Limestone dip slope and the British Geological
610 Society for the use of the photomontage of the high wall.



611 References

- 612 Andrews, B. J., Roberts, J. J., Shipton, Z. K., Bigi, S., Tartarello, M. C. and Johnson, G. O.: How do we
613 see fractures? Quantifying subjective bias in fracture data collection, *Solid Earth*, 10(2), 487–516,
614 doi:10.5194/se-2018-135, 2019.
- 615 Baptie, B.: Seismogenesis and state of stress in the UK, *Tectonophysics*, 482(1–4), 150–159,
616 doi:10.1016/j.tecto.2009.10.006, 2010. Bense, V. F., Gleeson, T., Loveless, S. E., Bour, O. and Scibek,
617 J.: Fault zone hydrogeology, *Earth-Science Rev.*, 127, 171–192, doi:10.1016/j.earscirev.2013.09.008,
618 2013.
- 619 Billi, A., Salvini, F. and Storti, F.: The damage zone-fault core transition in carbonate rocks: Implications
620 for fault growth, structure and permeability, *J. Struct. Geol.*, 25(11), 1779–1794, doi:10.1016/S0191-
621 8141(03)00037-3, 2003.
- 622 Bluck, B. J.: Pre-Carboniferous history of the Midland Valley of Scotland, *Trans. R. Soc. Edinb. Earth
623 Sci.*, 75(2), 275–295, doi:10.1017/S0263593300013900, 1984.
- 624 Browne, M. A. E. and Monro, S. K.: Evolution of the coal basins of Central Scotland, in *Congrès
625 International de Stratigraphie et de Géologie du Carbonifère*, pp. 1–19, Nanjing University Press, Nanjing,
626 Beijing., 1987.
- 627 Caine, J. S., Evans, J. P. and Forster, C. B.: Fault zone architecture and permeability structure, *Geology*,
628 24(11), 1025–1028, 1996.
- 629 Caputo, R.: Evolution of orthogonal sets of coeval extension joints, *Terra Nov.*, 7(5), 479–490,
630 doi:10.1111/j.1365-3121.1995.tb00549.x, 1995.
- 631 Caputo, R. and Hancock, P. L.: Crack-jump mechanism and its implications for stress cyclicity during
632 extension fracturing, *J. Geodyn.*, 27(1), 45–60, doi:10.1016/S0264-3707(97)00029-X, 1998.
- 633 Chang, C. and Haimson, B.: True triaxial strength and deformability of the German Continental Deep
634 Drilling Program (KTB) deep hole amphibolite, *J. Geophys. Res. Solid Earth*, 105(B8), 18999–19013,
635 doi:10.1029/2000jb900184, 2000.
- 636 Cherubini, Y., Cacace, M., Scheck-Wenderoth, M. and Noack, V.: Influence of major fault zones on 3-D
637 coupled fluid and heat transport for the Brandenburg region (NE German Basin), *Geotherm. Energy
638 Sci.*, 2(1), 1–20, doi:10.5194/gtes-2-1-2014, 2014.
- 639 Comerford, A., Fraser-Harris, A., Johnson, G. and McDermott, C. I.: Controls on geothermal heat
640 recovery from a hot sedimentary aquifer in Guardbridge, Scotland: Field measurements, modelling and
641 long term sustainability, *Geothermics*, 76, 125–140, doi:10.1016/j.geothermics.2018.07.004, 2018.
- 642 Crider, J. G. and Peacock, D. C. P.: Initiation of brittle faults in the upper crust: A review of field
643 observations, *J. Struct. Geol.*, 26(4), 691–707, doi:10.1016/j.jsg.2003.07.007, 2004.
- 644 Davis, A.: Carboniferous rocks of the Muirkirk, Gass Water and Glenmuir areas of Ayrshire, *Bull Geol
645 Surv GB*, 40, 1–49, 1972.



- 646 Dean, M. T., Browne, M. A. E., Waters, C. N. and Powell, J. H.: A lithostratigraphical framework for the
647 Carboniferous successions of northern Great Britain (onshore), *Br. Geol. Surv. Res. Rep.*, RR/10/07, 174,
648 2011.
- 649 Dershowitz, W. S. and Einstein, H. .: Characterizing Rock Joint Geometry with Joint System Models,
650 *Rock Mech. Rock Eng.*, 21(1), 21–51, 1988.
- 651 Donnelly, L. J.: A review of coal mining induced fault reactivation in Great Britain, *Q. J. Eng. Geol.*
652 *Hydrogeol.*, 39, 5–50, 2006.
- 653 Ellen, R.: Predicting the Internal Structure of Fault Zones in Basalt and its Effect on Along Fault-Fluid
654 Flow, University of Strathclyde., 2011.
- 655 Ellen, R., Callaghan, E., Leslie, A. G. and Browne, M. A. E.: The rocks of Spireslack surface coal mine
656 and its subsurface data: an introduction, *Br. Geol. Surv. Res. Rep.*, OR/16/053, 38, 2016.
- 657 Ellen, R., Browne, M. A. ., Mitten, A. ., Clarke, S. M., Leslie, A. G. and Callaghan, E.: Sedimentology,
658 architecture and depositional setting of the fluvial Spireslack Sandstone of the Midland Valley, Scotland:
659 insights from the Spireslack surface coal mine, *Geol. Soc. London, Spec. Publ.*, 488, SP488-2, 2019.
- 660 Ferrill, D. A. and Morris, A. P.: Dilational normal faults, *J. Struct. Geol.*, 25, 183–196,
661 doi:10.1016/S0191-8141(02)00196-7, 2003.
- 662 Ferrill, D. A. and Morris, A. P.: Fault zone deformation controlled by carbonate mechanical stratigraphy,
663 Balcones fault system, Texas, *Am. Assoc. Pet. Geol. Bull.*, 92(3), 359–380, doi:10.1306/10290707066,
664 2008.
- 665 Ferrill, D. A., McGinnis, R. N., Morris, A. P. and Smart, K. J.: Hybrid failure: Field evidence and
666 influence on fault refraction, *J. Struct. Geol.*, 42, 140–150, doi:10.1016/j.jsg.2012.05.012, 2012.
- 667 Ferrill, D. A., McGinnis, R. N., Morris, A. P., Smart, K. J., Sickmann, Z. T., Bentz, M., Lehrmann, D.
668 and Evans, M. A.: Control of mechanical stratigraphy on bed-restricted jointing and normal faulting:
669 Eagle Ford Formation, south-central Texas, *Am. Assoc. Pet. Geol. Bull.*, 98(11), 2477–2506,
670 doi:10.1306/08191414053, 2014.
- 671 Ferrill, D. A., Morris, A. P., McGinnis, R. N., Smart, K. J., Wigginton, S. S. and Hill, N. J.: Mechanical
672 stratigraphy and normal faulting, *J. Struct. Geol.*, 94, 275–302, doi:10.1016/j.jsg.2016.11.010, 2017.
- 673 Fossen, H. and Rotevatn, A.: Fault linkage and relay structures in extensional settings-A review, *Earth-*
674 *Science Rev.*, 154, 14–28, doi:10.1016/j.earscirev.2015.11.014, 2016.
- 675 Fowler, P. and Gayer, R. A.: The association between tectonic deformation , inorganic composition and
676 coal rank in the bituminous coals from the South Wales coalfield , United Kingdom, *Int. J. Coal Geol.*,
677 42, 1–31, 1999.
- 678 Francis, E. H.: Carboniferous: in CRAIG, in *The Geology of Scotland*, pp. 253–296, Scottish Academic
679 Press, Edinburgh., 1991.
- 680 Frodsham, K. and Gayer, R. A.: The impact of tectonic deformation upon coal seams in the South Wales



- 681 coalfield, UK, *Int. J. Coal Geol.*, 38(3–4), 297–332, doi:10.1016/S0166-5162(98)00028-7, 1999.
- 682 Gabrielsen, R. H., Braathen, A., Kjemperud, M. and Valdresbraten, M. L. R.: The geometry and
683 dimensions of fault-core lenses, *Geol. Soc. London, Spec. Publ.*, 439, 1–21, doi:10.1144/SP439.4, 2016.
- 684 Gamson, P. D., Beamish, B. B. and Johnson, D. P.: Coal microstructure and micropermeability and their
685 effects on natural gas recovery, *Fuel*, 72(1), 87–99, doi:10.1016/0016-2361(93)90381-B, 1993.
- 686 Godyń, K.: Structurally Altered Hard Coal in the Areas of Tectonic Disturbances – An Initial Attempt at
687 Classification, *Arch. Min. Sci.*, 61(3), 677–694, doi:10.1515/amsc-2016-0047, 2016.
- 688 Gross, M. R., Bahat, D. and Becker, A.: Relations between jointing and faulting based on fracture-spacing
689 ratios and fault-slip profiles: A new method to estimate strain in layered rocks, *Geology*, 25(10), 887–
690 890, doi:10.1130/0091-7613(1997)025<0887:RBJAFB>2.3.CO;2, 1997.
- 691 Gudmundsson, A., Simmenes, T. H., Larsen, B. and Philipp, S. L.: Effects of internal structure and local
692 stresses on fracture propagation, deflection, and arrest in fault zones, *J. Struct. Geol.*, 32, 1643–1655,
693 doi:10.1016/j.jsg.2009.08.013, 2010.
- 694 Haimson, B. and Chang, C.: A new true triaxial cell for testing mechanical properties of rock, and its use
695 to determine rock strength and deformability of Westerly granite, in *International Journal of Rock
696 Mechanics and Mining Sciences*, vol. 37, pp. 285–296, Elsevier Science Ltd., 2000.
- 697 Hancock, P. L. and Barka, A. A.: Kinematic indicators on active normal faults in Western Turkey, *J.
698 Struct. Geol.*, 9(5–6), 573–584, doi:10.1016/0191-8141(87)90142-8, 1987.
- 699 Healy, D., Jones, R. R. and Holdsworth, R. E.: Three-dimensional brittle shear fracturing by tensile crack
700 interaction, *Nature*, 439(7072), 64–67, doi:10.1038/nature04346, 2006.
- 701 Heidbach, O., Tingay, M., Barth, A., Reinecker, J., Kurfeß, D. and Müller, B.: The world stress map
702 database release, *WSM, Rel2008(9)* [online] Available from: doi: 10.1594/GFZ, 2008.
- 703 Ju, Y., Yan, Z., Li, X., Hou, Q., Zhang, W., Fang, L., Yu, L. and Wei, M.: Structural Characteristics and
704 Physical Properties of Tectonically Deformed Coals, *J. Geol. Res.*, 2012, 1–14,
705 doi:10.1155/2012/852945, 2012.
- 706 Lăpădat, A., Imber, J., Yielding, G., Iacopini, D., McCaffrey, K. J. W., Long, J. J. and Jones, R. R.:
707 Occurrence and development of folding related to normal faulting within a mechanically heterogeneous
708 sedimentary sequence: A case study from Inner Moray Firth, UK, in *Geological Society Special
709 Publication*, vol. 439, pp. 373–394, Geological Society of London., 2017.
- 710 Laubach, S. E., Marrett, R. A., Olson, I. E. and Scott, A. R.: Characteristics and origins of coal cleat: a
711 review, *Int. J. Coal Geol.*, 35(1–4), 175–207, doi:10.1016/S0166-5162(97)00012-8, 1998.
- 712 Laubach, S. E., Olson, J. E. and Cross, M. R.: Mechanical and fracture stratigraphy, *Am. Assoc. Pet.
713 Geol. Bull.*, 93(11), 1413–1426, doi:10.1306/07270909094, 2009.
- 714 Leeder, M. R.: Upper Palaeozoic basins of the British Isles-Caledonide inheritance versus Hercynian plate
715 margin processes, *J. Geol. Soc. London*, 139(1980), 479–491, doi:10.1144/gsjgs.139.4.0479, 1982.



- 716 Leeder, M. R.: Recent developments in Carboniferous geology: a critical review with implications for the
717 British Isles and N.W. Europe, *Proc. Geol. Assoc.*, 99(2), 79–100, 1988.
- 718 Lei, Q., Latham, J. P. and Tsang, C. F.: The use of discrete fracture networks for modelling coupled
719 geomechanical and hydrological behaviour of fractured rocks, *Comput. Geotech.*, 85, 151–176,
720 doi:10.1016/j.compgeo.2016.12.024, 2017.
- 721 Leslie, A. G., Browne, M. A. E., Cain, T. and Ellen, R.: From threat to future asset—The legacy of
722 opencast surface-mined coal in Scotland, *Int. J. Coal Geol.*, 164, 123–133,
723 doi:10.1016/j.coal.2016.06.017, 2016.
- 724 Li, H.: Major and minor structural features of a bedding shear zone along a coal seam and related gas
725 outburst, Pingdingshan coalfield, northern China, *Int. J. Coal Geol.*, 47, 101–113, 2001.
- 726 Li, W., Ren, T., Busch, A., den Hartog, S. A. M., Cheng, Y., Qiao, W. and Li, B.: Architecture, stress
727 state and permeability of a fault zone in Jiulishan coal mine, China: Implication for coal and gas outbursts,
728 *Int. J. Coal Geol.*, 198, 1–13, doi:10.1016/j.coal.2018.09.002, 2018.
- 729 Li, Y. W., Zhang, J. and Liu, Y.: Effects of loading direction on failure load test results for Brazilian tests
730 on coal rock, *Rock Mech. Rock Eng.*, 49(6), 2173–2180, doi:10.1007/s00603-015-0841-8, 2016.
- 731 Lohr, T., Krawczyk, C. M., Oncken, O. and Tanner, D. C.: Evolution of a fault surface from 3D attribute
732 analysis and displacement measurements, *J. Struct. Geol.*, 30(6), 690–700, doi:10.1016/j.jsg.2008.02.009,
733 2008.
- 734 Long, J. J. and Imber, J.: Geological controls on fault relay zone scaling, *J. Struct. Geol.*, 33(12), 1790–
735 1800, doi:10.1016/j.jsg.2011.09.011, 2011.
- 736 Lunn, R. J., Willson, J. P., Shipton, Z. K. and Moir, H.: Simulating brittle fault growth from linkage of
737 preexisting structures, *J. Geophys. Res. Solid Earth*, 113(7), doi:10.1029/2007JB005388, 2008.
- 738 Malolepszy, Z.: Man-made, low-temperature reservoirs in abandoned workings of underground mines on
739 example of Nowa Ruda coal mine, Poland, in *International Geothermal Conference*, pp. 23–29,
740 Reykjavík., 2003.
- 741 Manzocchi, T.: The connectivity of two-dimensional networks of spatially correlated fractures, *Water*
742 *Resour. Res.*, 38(9), 1-1-1–20, doi:10.1029/2000WR000180, 2002.
- 743 Min, K. B., Jing, L. and Stephansson, O.: Determining the equivalent permeability tensor for fractured
744 rock masses using a stochastic REV approach: Method and application to the field data from Sellafeld,
745 UK, *Hydrogeol. J.*, 12(5), 497–510, doi:10.1007/s10040-004-0331-7, 2004.
- 746 Moir, H.: *Modelling fault zone evolution : the effect of heterogeneity*, University of Strathclyde., 2010.
- 747 Moir, H., Lunn, R. J., Shipton, Z. K. and Kirkpatrick, J. D.: Simulating brittle fault evolution from
748 networks of pre-existing joints within crystalline rock, *J. Struct. Geol.*, 32(11), 1742–1753,
749 doi:10.1016/j.jsg.2009.08.016, 2010.
- 750 Monaghan, A. : *The Carboniferous shales of the Midland Valley of Scotland : geology and resource*



- 751 estimation, British Geological Survey for Department of Energy and Climate Change, London, UK.,
752 2014.
- 753 Nemser, E. S. and Cowan, D. S.: Downdip segmentation of strike-slip fault zones in the brittle crust,
754 *Geology*, 37(5), 419–422, doi:10.1130/G25619A.1, 2009.
- 755 Nicol, A., Watterson, J., Walsh, J. J. and Childs, C.: The shapes, major axis orientations and displacement
756 patterns of fault surfaces, *J. Struct. Geol.*, 18(2–3), 235–248, doi:10.1016/S0191-8141(96)80047-2, 1996.
- 757 Nyberg, B., Nixon, C. W. and Sanderson, D. J.: NetworkGT: A GIS tool for geometric and topological
758 analysis of two-dimensional fracture networks, *Geosphere*, 14(4), 1618–1634, doi:10.1130/GES01595.1,
759 2018.
- 760 Nygård, R., Gutierrez, M., Bratli, R. K. and Høeg, K.: Brittle-ductile transition, shear failure and leakage
761 in shales and mudrocks, *Mar. Pet. Geol.*, 23(2), 201–212, doi:10.1016/j.marpetgeo.2005.10.001, 2006.
- 762 Peacock, D. C. P.: The temporal relationship between joints and faults, *J. Struct. Geol.*, 23(2–3), 329–
763 341, doi:10.1016/S0191-8141(00)00099-7, 2001.
- 764 Peacock, D. C. P., Sanderson, D. J. and Rotevatn, A.: Relationships between fractures, *J. Struct. Geol.*,
765 106, 41–53, doi:10.1016/j.jsg.2017.11.010, 2018.
- 766 Priest, S. D. and Hudson, J. A.: Estimation of discontinuity spacing and trace length using scanline
767 surveys, *Int. J. Rock Mech. Min. Sci.*, 18(3), 183–197, doi:10.1016/0148-9062(81)90973-6, 1981.
- 768 Rippon, J., Read, W. A. and Park, R. G.: The Ochil Fault and the Kincardine basin: Key structures in the
769 tectonic evolution of the Midland Valley of Scotland, *J. Geol. Soc. London.*, 153(4), 573–587,
770 doi:10.1144/gsjgs.153.4.0573, 1996.
- 771 Ritchie, J. D., Johnson, H., Browne, M. A. E. and Monaghan, A. A.: Late Devonian-Carboniferous
772 tectonic evolution within the Firth of Forth, Midland Valley: As revealed from 2D seismic reflection data,
773 *Scottish J. Geol.*, 39(2), 121–134, doi:10.1144/sjg39020121, 2003.
- 774 Roche, V., Homberg, C. and Rocher, M.: Fault nucleation, restriction, and aspect ratio in layered sections:
775 Quantification of the strength and stiffness roles using numerical modeling, *J. Geophys. Res. Solid Earth*,
776 118, 4446–4460, 2013.
- 777 Rohrbaugh, J. B., Dunne, W. M. and Mauldon, M.: Estimating fracture trace intensity, density, and mean
778 length using circular scan lines and windows, *Am. Assoc. Pet. Geol. Bull.*, 86(12), 2089–2104,
779 doi:10.1306/61EEDE0E-173E-11D7-8645000102C1865D, 2002.
- 780 Sagy, A., Brodsky, E. E. and Axen, G. J.: Evolution of fault surface roughness with slip, *Geology*, 35(3),
781 283–286, doi:10.1130/G23235A.1, 2007.
- 782 Sanderson, D. J.: Field-based structural studies as analogues to sub-surface reservoirs, in *Geological*
783 *Society Special Publication*, vol. 436, pp. 207–217, Geological Society of London., 2015.
- 784 Sanderson, D. J. and Nixon, C. W.: The use of topology in fracture network characterization, *J. Struct.*
785 *Geol.*, 72, 55–66, doi:10.1016/j.jsg.2015.01.005, 2015.



- 786 Sanderson, D. J. and Nixon, C. W.: Topology, connectivity and percolation in fracture networks, *J. Struct. Geol.*, 115(August 2016), 167–177, doi:10.1016/j.jsg.2018.07.011, 2018.
- 788 Scheiber, T., Fredin, O., Viola, G., Jarna, A., Gasser, D. and Łapińska-viola, R.: Manual extraction of
789 bedrock lineaments from high-resolution LiDAR data : methodological bias and human perception, *GFF*,
790 137(4), doi:10.1080/11035897.2015.1085434, 2015.
- 791 Schmatz, J., Vrolijk, P. J. and Urai, J. L.: Clay smear in normal fault zones - The effect of multilayers and
792 clay cementation in water-saturated model experiments, *J. Struct. Geol.*, 32(11), 1834–1849,
793 doi:10.1016/j.jsg.2009.12.006, 2010.
- 794 Schöpfer, M. P. J., Childs, C. and Walsh, J. J.: Two-dimensional distinct element modeling of the structure
795 and growth of normal faults in multilayer sequences: 2. Impact of confining pressure and strength contrast
796 on fault zone geometry and growth, *J. Geophys. Res. Solid Earth*, 112(10), doi:10.1029/2006JB004903,
797 2007.
- 798 Schöpfer, M. P. J., Childs, C., Walsh, J. J. and Manzocchi, T.: Evolution of the internal structure of fault
799 zones in three-dimensional numerical models of normal faults, *Tectonophysics*, 666, 158–163,
800 doi:10.1016/j.tecto.2015.11.003, 2016.
- 801 Shuichang, Z., Jingkui, M., Liuhong, L. and Shizhen, T.: Geological features and formation of coal-
802 formed tight sandstone gas pools in China: Cases from Upper Paleozoic gas pools, Ordos Basin and
803 Xujiahe Formation gas pools, Sichuan Basin, *Pet. Explor. Dev.*, 36(3), 320–330, doi:10.1016/S1876-
804 3804(09)60129-4, 2009.
- 805 Sibson, R. H.: Conditions for fault-valve behaviour, edited by R. J. Knipe and E. . Rutter, *Geol. Soc.
806 London, Spec. Publ.*, 54(1), 15–28, doi:10.1144/GSL.SP.1990.054.01.02, 1990.
- 807 Sibson, R. H.: Implications of fault-valve behaviour for rupture nucleation and recurrence,
808 *Tectonophysics*, 211(1–4), 283–293, doi:10.1016/0040-1951(92)90065-E, 1992.
- 809 Soden, A. M. and Shipton, Z. K.: Dilational fault zone architecture in a welded ignimbrite: The
810 importance of mechanical stratigraphy, *J. Struct. Geol.*, 51, 156–166, doi:10.1016/j.jsg.2013.02.001,
811 2013.
- 812 Soden, A. M., Shipton, Z. K., Lunn, R. J., Pytharouli, S. I., Kirkpatrick, J. D., Do Nascimento, A. F. and
813 Bezerra, F. H. R.: Brittle structures focused on subtle crustal heterogeneities: implications for flow in
814 fractured rocks, *J. Geol. Soc. London.*, 171(4), 509–524, doi:10.1144/jgs2013-051, 2014.
- 815 Soliva, R. and Benedicto, A.: Geometry, scaling relations and spacing of vertically restricted normal
816 faults, *J. Struct. Geol.*, 27(2), 317–325, doi:10.1016/j.jsg.2004.08.010, 2005.
- 817 Solomon, S.: Carbon Dioxide Storage: Geological Security and Environmental Issues-Case Study on the
818 Sleipner Gas field in Norway, *Bellona Rep.*, 128, 2007.
- 819 Sylvester, A. G.: Strike-slip faults, *Bull. Geol. Soc. Am.*, 100(11), 1666–1703, doi:10.1130/0016-
820 7606(1988)100<1666:SSF>2.3.CO;2, 1988.
- 821 Thomas, L.: *Coal Geology, Second.*, Wiley-Blackwell, Chichester., 2013.



- 822 Underhill, J. R., Monaghan, A. A. and Browne, M. A. E.: Controls on structural styles, basin development
823 and petroleum prospectivity in the Midland Valley of Scotland, *Mar. Pet. Geol.*, 25(10), 1000–1022,
824 doi:10.1016/j.marpetgeo.2007.12.002, 2008.
- 825 Walsh, J. J., Nicol, A. and Childs, C.: An alternative model for the growth of faults, *J. Struct. Geol.*,
826 24(11), 1669–1675, doi:10.1016/S0191-8141(01)00165-1, 2002.
- 827 Wang, F. P. and Gale, G. F. .: Screening Criteria for Shale-Gas Systems, *Gulf Coast Assoc Geol Soc*
828 *Trans.*, 59, 779–93, 2009.
- 829 Whittles, D. N., Yasar, E., Reddish, D. J. and Lloyd, P. W.: Anisotropic strength and stiffness properties
830 of some UK coal measure siltstones, *Q. J. Eng. Geol. Hydrogeol.*, 35(2), 155–166, doi:10.1144/1470-
831 9236/1999-29, 2002.
- 832 Wibberley, C. A. J., Yielding, G., Giulio, &, Toro, D. and Di Toro, G.: Recent advances in the
833 understanding of fault zone internal structure: a review, Wibberley, C. A. J., Kurz, W., Imber, J.,
834 Holdsworth, R. E. Collett. C. (eds). *Intern. Struct. fault Zo. Implic. Mech. fluid-flow Prop. Geol. Soc.*
835 *London, Spec. Publ.*, 299(1), 5–33, doi:10.1144/SP299.2, 2008.
- 836 Wilkins, S. J. and Gross, M. R.: Normal fault growth in layered rocks at Split Mountain, Utah: Influence
837 of mechanical stratigraphy on dip linkage, fault restriction and fault scaling, *J. Struct. Geol.*, 24(9), 1413–
838 1429, doi:10.1016/S0191-8141(01)00154-7, 2002.
- 839 Wilkins, S. J., Gross, M. R., Wacker, M., Eyal, Y. and Engelder, T.: Faulted joints: Kinematics,
840 displacement-length scaling relations and criteria for their identification, *J. Struct. Geol.*, 23(2–3), 315–
841 327, doi:10.1016/S0191-8141(00)00098-5, 2001.
- 842 Wright, T. D. and Turner, J. P.: Characterization of 3D fault curvature., 2006.
- 843 Yuan, Y. S., Jin, Z. J., Zhou, Y., Liu, J. X., Li, S. J. and Liu, Q. Y.: Burial depth interval of the shale
844 brittle–ductile transition zone and its implications in shale gas exploration and production, *Pet. Sci.*, 14(4),
845 637–647, doi:10.1007/s12182-017-0189-7, 2017.
- 846 van der Zee, W. and Urai, J. L.: Processes of normal fault evolution in a siliciclastic sequence: A case
847 study from Miri, Sarawak, Malaysia, *J. Struct. Geol.*, 27(12), 2281–2300, doi:10.1016/j.jsg.2005.07.006,
848 2005.
- 849